CSIRO MARINE LABORATORIES
Report 227

A Global Ocean General Circulation Model for Climate Variability Studies

A. Schiller, J. S. Godfrey, P. McIntosh and G. Meyers

1997

Bibliography. ISBN 0 643 05959 8.

1. Hydrodynamic weather forecasting - Australia -
Mathematical models. 2. Ocean circulation - Australia -
Mathematical models. 3. Ocean-atmosphere interaction -
Australia - Mathematical models. I. Schiller, Andreas, 1960 -.
II. CSIRO. Marine Laboratories. (Series : Report
(CSIRO. Marine Laboratories); 227).

551.63015118

Contents

1 Introduction

Over the last twenty years or so, scientists have started using sophisticated computer models to examine the way our climate is likely to change in the future. Although science has made considerable progress in seasonal forecasting, at this stage detailed and accurate forecasts of the climate a few months ahead are still strongly dependent on what parameterisations are used in the models. However, short-term forecasts up to a few years will, hopefully, soon become more accurate as the performance of numerical models of the ocean and atmosphere is improved.

Several studies (e.g. Neelin et al. 1992; Stockdale et al. 1993; Mechoso et al. 1995) have recently indicated that much of the climatic variability on seasonal to interannual time-scales results from interactions of the world ocean and the atmosphere. Due to its large heat capacity, the ocean plays a crucial role in coupled models since it modulates the interannual variations of the climate system.

The predominantly subtropical position of the Australian continent makes it susceptible to extremes of climate (such as droughts and floods) caused by interactions and feedbacks of the ocean and the atmosphere. Furthermore, climate changes on seasonal to interannual time-scales like ENSO (El Niño – Southern Oscillation) can have major impacts on Australia's climate, with El Niño generally corresponding to dry periods in eastern and northern Australia. The opposite La Niña event causes rather wet spells, with occasional floods in Queensland. While the correlation between rainfall in Queensland and ENSO in the Pacific is high, rainfall in much of the rest of Australia cannot be forecast by ENSO alone. In the southeastern and western states, it is strongly correlated to sea-surface temperature (SST) in the Indian Ocean (Nicholls 1989; Drosdowsky 1993).

SST affects all maritime atmospheric processes, and determines the extent of atmospheric convection and monsoon rain in tropical regions. In particular, sea-surface temperature and the ocean's associated thermocline structure in the western Pacific and eastern Indian oceans have a significant impact on Australia's climate, with patterns of rainfall over Australia showing a stronger relationship to SST in these regions than to the El Niño signal in the eastern Pacific.

To obtain forecasts for Australia's climate the development of a coupled ocean-atmosphere numerical circulation model is being developed jointly by Australia's CSIRO (Divisions of Atmospheric Research and Marine Research) and the Bureau of Meteorology. Their cooperation has been formally established under the auspices of a grant from the Land and Water Resources Research and Development Corporation. This project aims to improve

Vertical structure			
k	*mid-depth*	*level thickness*	*depth of bottom*
1	7.5	15.00	15.00
2	22.5	15.00	30.00
3	37.5	15.00	45.00
4	52.5	15.00	60.00
5	67.5	15.00	75.00
6	82.5	15.00	90.00
7	97.5	15.00	105.00
8	112.5	15.00	120.00
9	127.5	15.12	135.12
10	142.74	15.44	150.56
11	158.38	16.19	166.75
12	175.12	17.91	184.66
13	194.20	21.57	206.23
14	218.26	28.86	235.09
15	251.92	42.48	277.57
16	303.22	66.28	343.85
17	384.48	105.12	448.97
18	513.46	164.22	613.19
19	712.92	247.83	861.02
20	1009.12	357.34	1218.36
21	1427.60	489.36	1707.72
22	1987.84	634.44	2342.16
23	2696.48	777.32	3119.48
24	3542.48	899.14	4018.62
25	4494.76	981.38	5000.00

Table 2.2: Vertical temperature grid: mid-depth, level thickness and depth at the bottom of each level in m.
k is the vertical grid index.

The bathymetry of the model (Fig. 2.1) represents a smoothed approximation to the high-resolution data set of Gates and Nelson (1975). To simulate the Indonesian Throughflow we modified the model's topography in that area, allowing for a transport of water masses through Lombok Strait and the Timor Sea. Because islands are computationally expensive in this version of the the GFDL model, only the Philippines, Kalimantan, Celebes, the Lombok–Flores islands, Australia (combined with New Guinea), New Zealand and Antarctica are separated from the remaining land points (Fig.2.2). There is no Bering or Torres Strait. The Drake Passage was artificially widened to aid throughflow of the Antarctic Circumpolar Current.

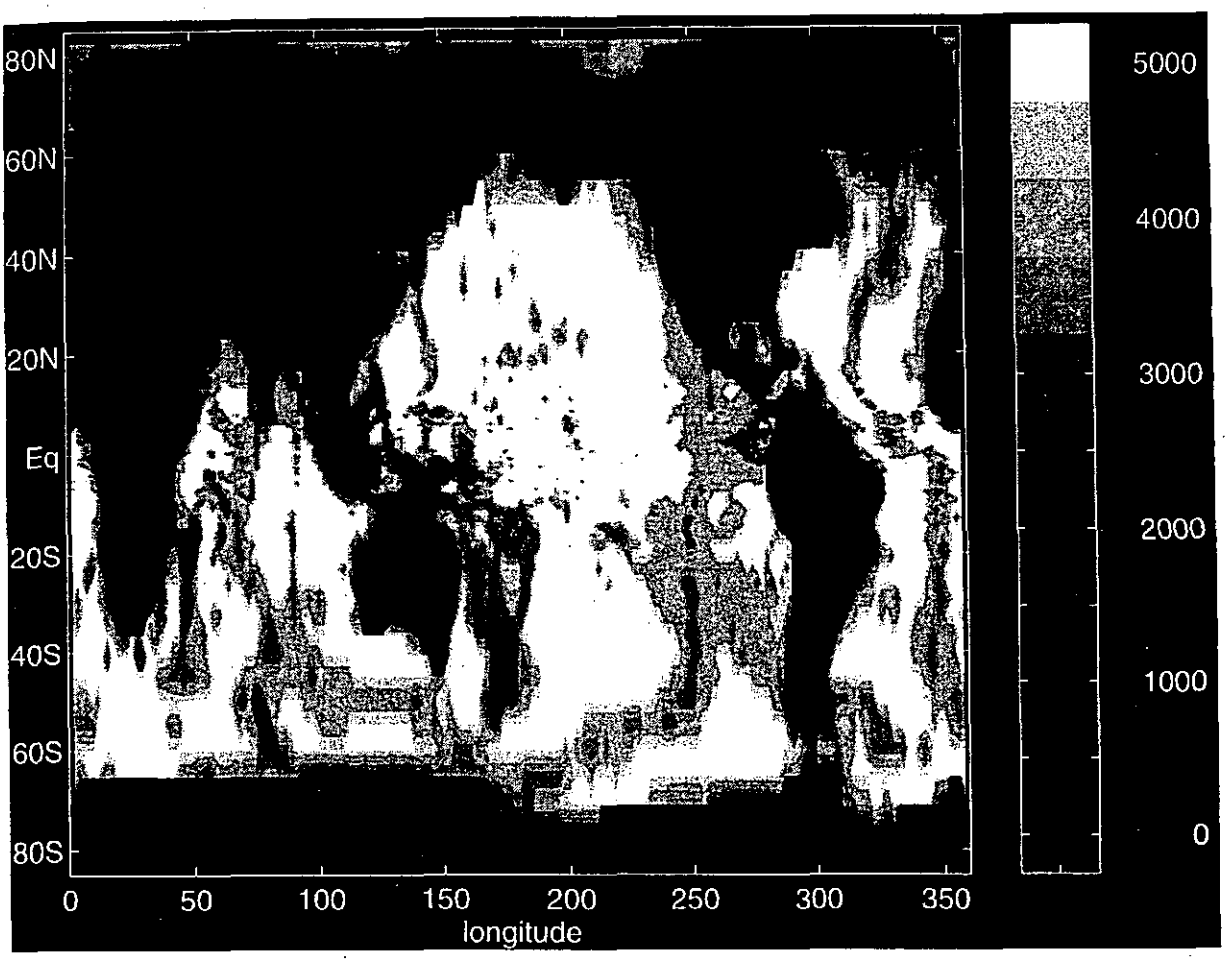

Figure 2.1: The bathymetry used in the model (m), based on Gates and Nelson (1975)

The flows of the Red Sea into the Indian Ocean and the Mediterranean Sea into the Atlantic Ocean significantly change the water-mass structures of these oceans. Because the Red and Mediterranean seas are not included in our model, their effects on the oceans are simulated by restoring temperature and salinity to observed values (Levitus 1982) at the lateral boundaries between the respective seas and oceans over the whole water depth.

Due to the strong changes in grid sizes in the model (enhanced tropical grid and coarse resolution close to the poles), and in order to guarantee numerical stability, the zonal and meridional viscosities are dependent on latitude. The modifications are similar to those Power et al. (1995) applied to another version of the model. The meridional viscosity is set to $2.0 \times 10^3\,\mathrm{m}^2/\mathrm{s}$ near the equator but then increases to over $3.1 \times 10^5\,\mathrm{m}^2/\mathrm{s}$ at high latitudes, while the zonal viscosity is $2.0 \times 10^4\,\mathrm{m}^2/\mathrm{s}$ near the equator but also increases to over $3.1 \times 10^5\,\mathrm{m}^2/\mathrm{s}$ at high latitudes. The horizontal diffusivity is set to $4.0 \times 10^3\,\mathrm{m}^2/\mathrm{s}$ everywhere.

3 Surface-flux formulations

As noted in the Introduction, a major aim of the Division of Marine Research component of the project is to test the ability of our OGCM — when driven with an observationally based estimate of interannual fluxes — to simulate observed interannual SST anomalies. For this purpose, we have generated interannually varying estimates of the various fluxes for the period 1985-1990 (this period was the only one for which satellite-based shortwave radiation estimates were available). We have formed mean seasonal cycles of each flux, and used them in the runs discussed in this report. Later, we will conduct runs with the full observed interannual fluxes included.

The fluxes have been obtained as follows:

3.1 Momentum fluxes

We have used the monthly mean Florida State University (FSU) "pseudostresses" for 1985–1990 (Legler et al. 1989; Stricherz et al. 1992), with a constant bulk transfer coefficient C_D of 0.0015 (see Section 8, below). The mean seasonal cycle of wind stress has been constructed from these data. The FSU winds are only available in about 30°N–30°S; poleward of these latitudes, we blend into Hellerman and Rosenstein's (1983) seasonal mean wind stresses. To avoid inhomogenities in the transition regions, we blended over three grid points in each direction, which covers 6 degrees of longitude and approximately 10 degress of latitude. Figure 3.1 shows the annual mean curl of the wind stress based on the composed data set.

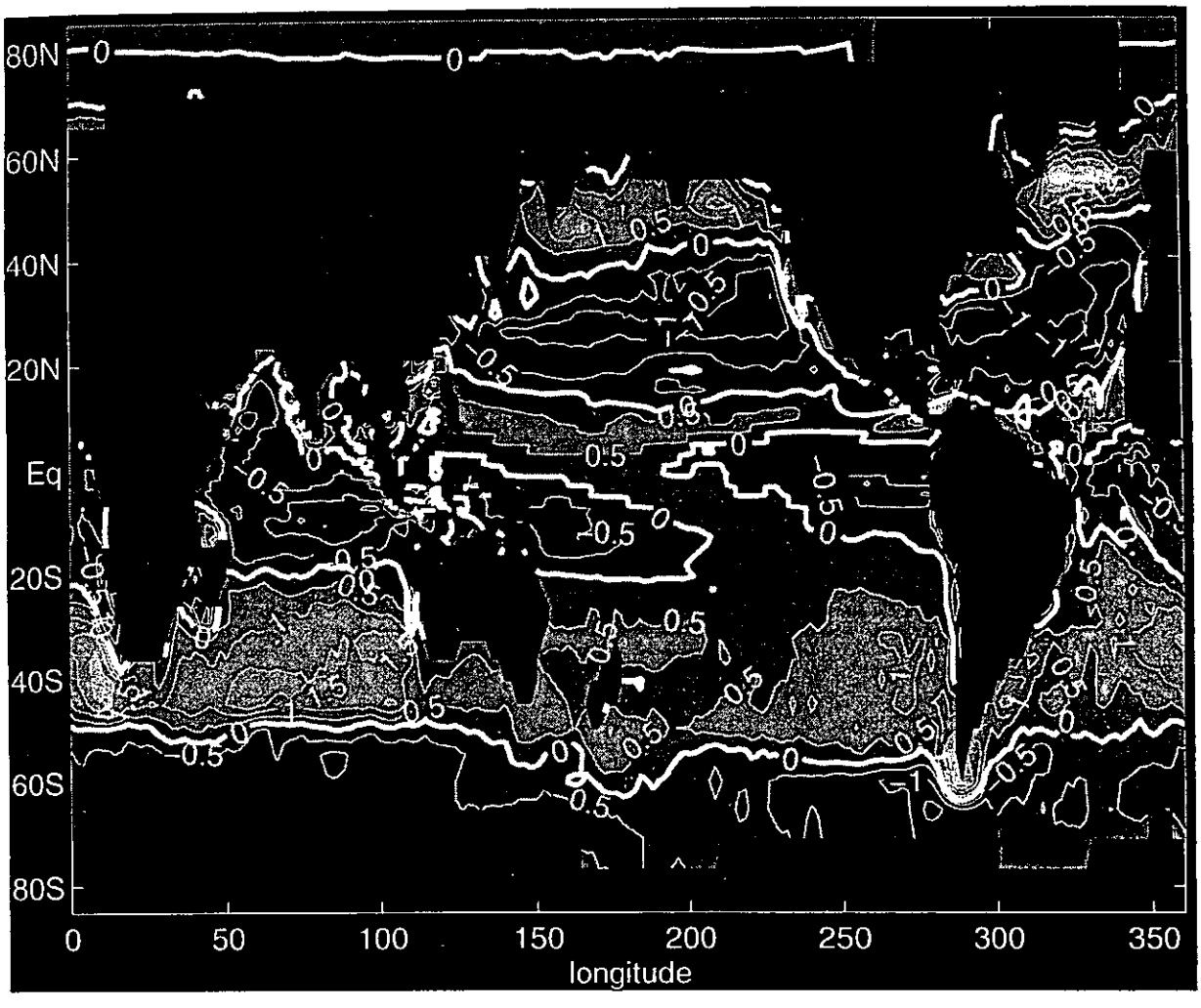

Figure 3.1: Annual mean curl of the wind stress (10^{-7} N/m^2), based on Florida State University (Legler et al. 1989; Stricherz et al. 1992) and Hellerman and Rosenstein (1983) data.

3.2 Freshwater fluxes

Rather than attempting to estimate interannual variations of freshwater fluxes, we simply allow the surface layer of the model (15 m deep) to relax to observed seasonal mean surface salinity, with a time constant of 17 days. The surface salinities are taken from Levitus (1982).

3.3 Heat fluxes

Particular attention was paid to the choice of the surface heat-flux boundary condition. The rationale for our choice is discussed in detail in Godfrey and Schiller (1997). The net heat flux is given by the formula:

$$
\begin{aligned}
Q_{tot} &= R_s \\
&+ \rho_a C_E L_v W (0.98 - \delta) q_{sat}(T_s) \\
&+ \alpha'(T_s - T^*) \\
&+ Q_{correct}
\end{aligned}
\tag{3.1}
$$

where R_s is the ISCCP "bulk" estimate of net upward shortwave radiation (Li 1995). This formula is closely related to those used by Seager et al. (1988) and Chen et al. (1994b). Q_{tot} is further separated into:

$$
Q_{tot} = Q_{surface} + Q_{penetrating} \tag{3.2}
$$

The latter term is assumed to fall off exponentially with depth, with a decay rate that varies with position according to empirical estimates of turbidity (Simonot and Le Treut 1986).

The second term on the right of (3.1) corresponds to latent heat exchange, and ρ_a, C_E and L_v, are air density, bulk-transfer coefficient and latent heat of vaporisation respectively. W is an estimate of wind speed — we take $W^2 = |\tau|^2 + W_0^2$, where $|\tau|$ is the magnitude of the monthly mean FSU wind pseudostress estimate and W_0 is a "gustiness estimate". We take $W_0 = 3\,m\,s^{-1}$.

In (3.1), $q_{sat}(T_s)$ is the saturated water-vapour pressure over freshwater at temperature T_s. The factor 0.98 accounts for ocean salinity. We choose $\delta = 0.75$, i.e. we assume that the marine-atmosphere boundary layer has a specific humidity that is a constant fraction δ of the saturated value at the (model) value T_s of SST.

The third term on the right of (3.1) represents the sum of sensible heat exchange and net longwave radiation, with $\alpha = 1.5\,W/m^2/°C$. According to the Oberhuber (1988) climatology, this sum is climatologically rather constant at roughly 55 W/m^2 over the tropical Pacific and Indian oceans. We choose $T^* = -8\,°C$, so that at a typical tropical SST of 28 °C, the third term $\alpha'(T_s - T^*)$ is $54\,W/m^2$. This representation of the sum of sensible heat exchange and longwave radiation is certainly accurate within the errors of order $20\,W/m^2$ or more in these estimates.

The last term in (3.1) represents a "flux correction", which must be added because the SST damping rate $\partial Q_{tot}/\partial T_s$ is so small: it is about $15\,W/m^2/°C$ for typical wind speeds with the constants given above. Thus a consistent error of $30\,W/m^2$ (which may

be present in the shortwave radiation product, e.g. Chen et al. 1994b) will lead to an unacceptable SST error of 2 °C.

We have obtained the flux correction $Q_{correct}$ by:

(a) estimating a mean seasonal cycle of R_s for the period 1985–1990, from the ISCCP product.

(b) estimating the mean seasonal cycle of SST, $T_{Reyn-seas}$, from the Reynolds SST product (Reynolds 1988; Reynolds and Smith 1994) for the same period 1985–1990;

(c) estimating the mean seasonal cycle of W for 1985–1990, from FSU winds.

We then run our OGCM with (3.1), but with $Q_{correct}$ replaced by $\lambda(T_{model} - T_{Reyn-seas})$, and λ an artificially large damping coefficient of $100\,W/m^2/°C$. With this choice, typical expected maximum flux errors of up to $50\,W/m^2$ and typical maximum SST errors of up to 0.5 °C will contribute about equally. During the last year of the spin-up integration of the model the monthly averages of $\lambda(T_{model} - T_{Reyn-seas})$ have been stored. These estimates of $Q_{correct}$ are used in (3.1) for runs to test the OGCM's ability to simulate interannual SST anomalies. Tests of this formulation with the IMET time series of heat fluxes are described in Godfrey and Schiller (1997).

3.4 Flux corrections

Figure 3.2a shows $Q_{correct}$, averaged over year 22 (2 years after tidal mixing was incorporated into the Indonesian region). Figure 3.2a divided by 100 is also a map of the departure of model SST over year 22 from the Reynolds annual mean. With this interpretation, one sees that the model's SST were within 0.5 °C of observed values over almost the entire tropical band (20°N–20°S) but that departures of up to 3 °C occur in small patches in western boundary currents, and in the Antarctic Circumpolar Current. These correspond to values of $Q_{correct}$ that are well over the $50\,W/m^2$ thought to be the maximum error in observed heat-flux climatologies.

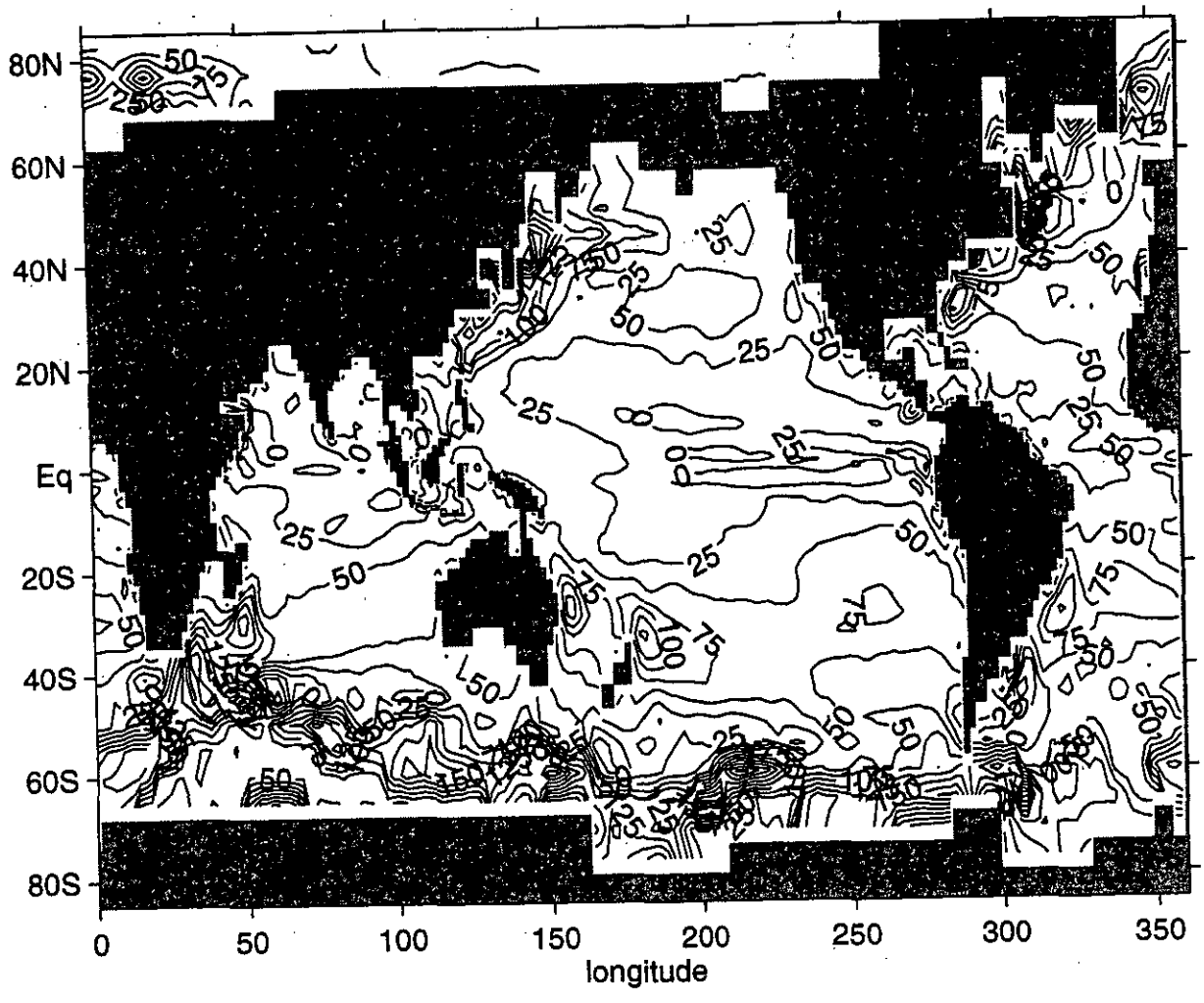

Figure 3.2a: Heat-flux correction, $Q_{correct}$ (W/m^2). These numbers, divided by 100, are also the difference between observed and modelled annual mean SST.

At this stage, we plan to continue with interannual runs despite the large size of these flux corrections, on the grounds that:

(a) in the tropical band of greatest importance, the flux corrections are not too large (they are generally less than $50\,W/m^2$ throughout the latitude band 20°N–20°S where SST anomalies are believed to have the greatest effect on the atmosphere); and

(b) experience shows that interannual anomalies of fluxes are often quite good, even when the long-term means contain large errors.

Nevertheless, the large size of the corrections in Figure 3.2a is disturbing, so they are now discussed further, with a possible view to correcting them after our first interannual runs.

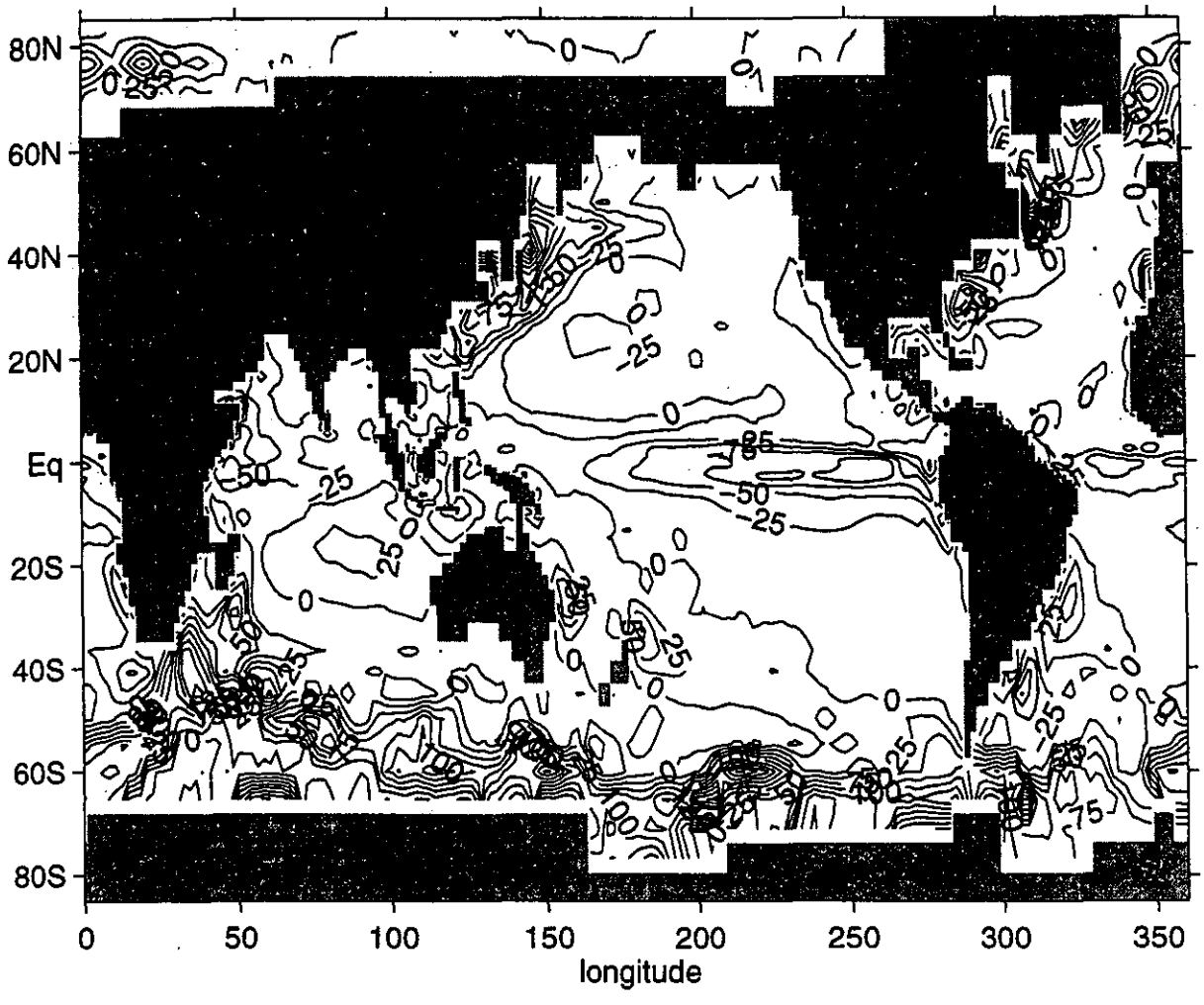

Figure 3.2b: Annual mean net heat flux Q_{tot} into the model (W/m^2).

$Q_{correct}$ is the difference between the net heat flux into the model (Fig. 3.2b) and the heat flux Q_{Seager} provided by the first three terms of (3.1) (Fig. 3.2c). Figure 3.2b is the heat flux required to bring the model currents to the model temperature in the top layer (i.e. Figure 3.2b is set by SST and oceanic processes in the model. Compared with observed climatologies such as Oberhuber's (1988) (Fig. 3.2d), the pattern of Figure 3.2b is fairly realistic. For example, Oberhuber (and other climatologies) show a maximum heat flux into the ocean of over $100\,W/m^2$ near $(0°, 250°E)$, which is similar to the value in Figure 3.2b. Similarly Oberhuber shows a maximum heat gain of $75\,W/m^2$ off equatorial east Africa, compared to over $50\,W/m^2$ in the model. The model underestimates the heat losses from the Agulhas Current and Gulf Stream regions.

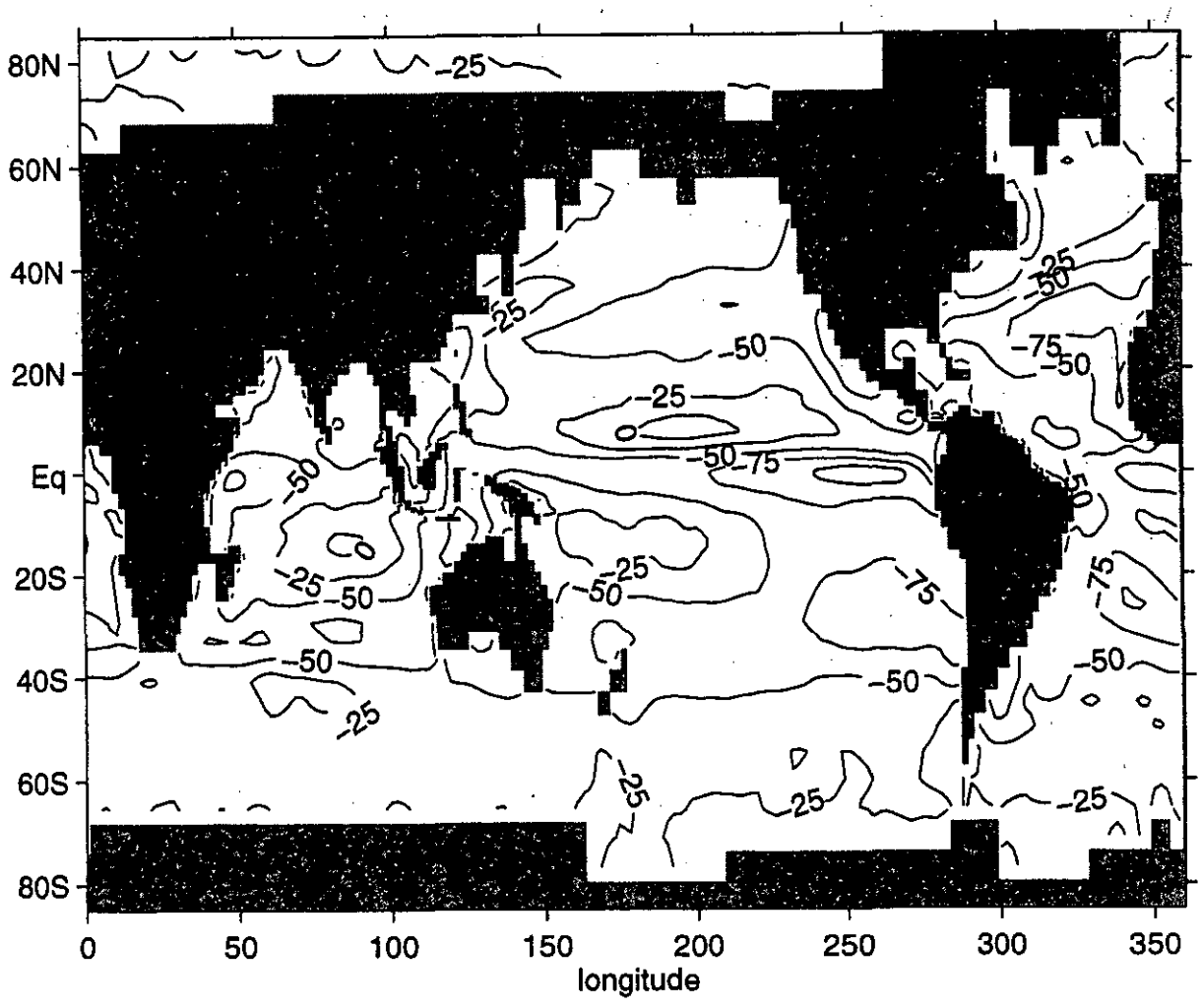

Figure 3.2c: Annual mean heat flux from the first three terms on the right of Eqn. (3.1), for the model (W/m^2).

In contrast, Figure 3.2c (the "Seager heat flux") is primarily determined by the ISCCP shortwave radiation product, and by FSU winds. It is also determined by the model's SST, but the form of (3.2) above is such that replacing model SST with observed SST (errors typically O(0.5°–1 °C), see Fig. 3.2a) will not affect the result much. Thus Figure 3.2b is effectively independent of the ocean model, and can be regarded as a crude observationally based heat-flux climatology.

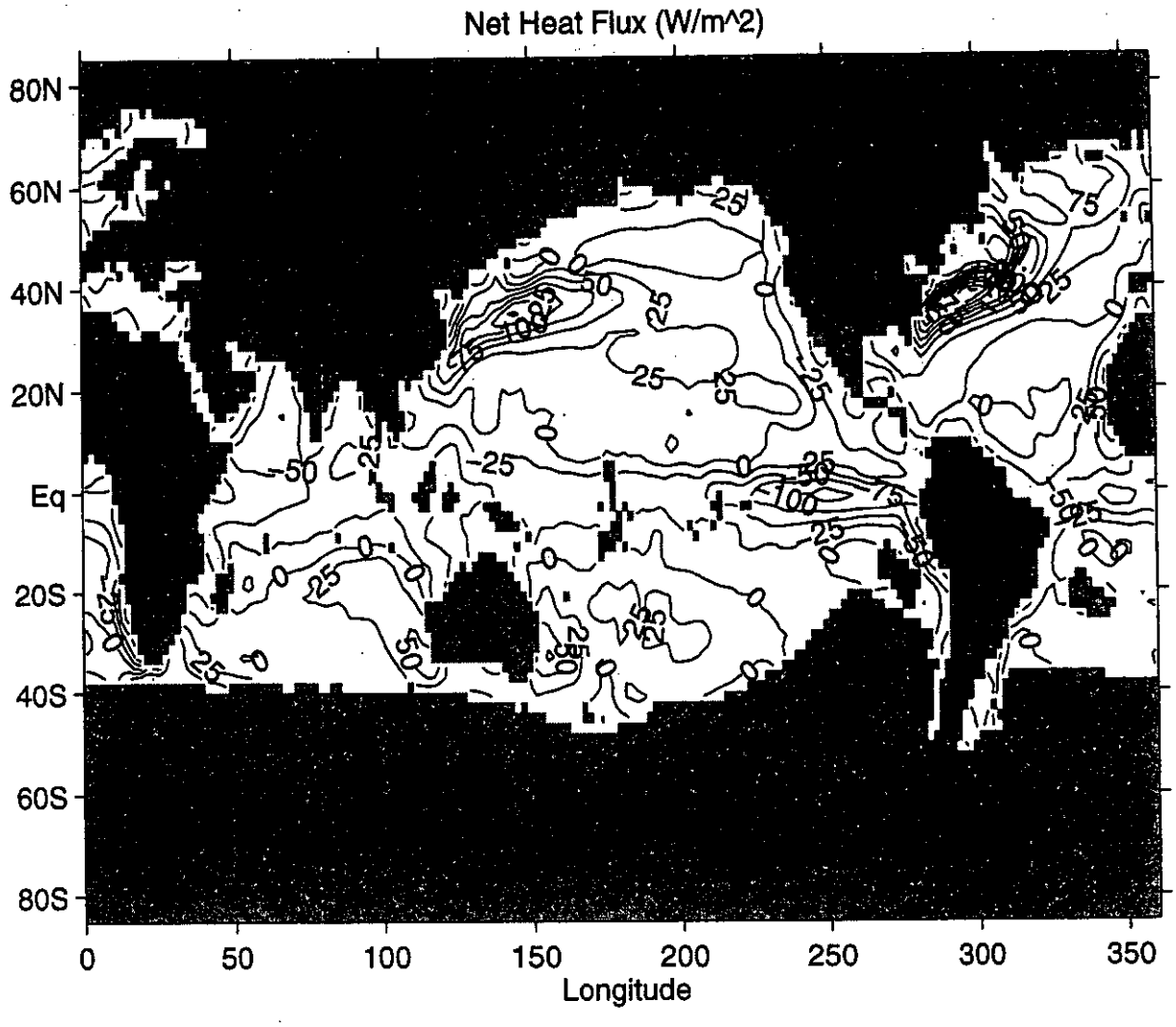

Figure 3.2d: Observed annual mean net heat flux into the ocean (Oberhuber 1988), in (W/m^2).

Comparing Figure 3.2c with climatologies such as Oberhuber's (1988) (Fig. 3.2d) reveals severe deficiencies. First, the heat fluxes in Figure 3.2c are negative (ocean gaining heat) almost everywhere. Secondly, the Kuroshio and Gulf Stream western boundary currents have hardly any net heat loss. These differences relate partly to the fact that the shortwave radiation product (Fig. 3.3a) is too strong (at least relative to Oberhuber, Figure 3.3b) over most of the globe, by perhaps 25–50 W/m^2. Secondly, the modelled latent heat loss (Fig. 3.4a), while quite similar to Oberhuber climatology in the tropics (Fig. 3.4b), does not contain the intense maxima in the Gulf Stream and Kuroshio seen in Figure 3.4b. This is because a constant factor δ was chosen in (3.1).

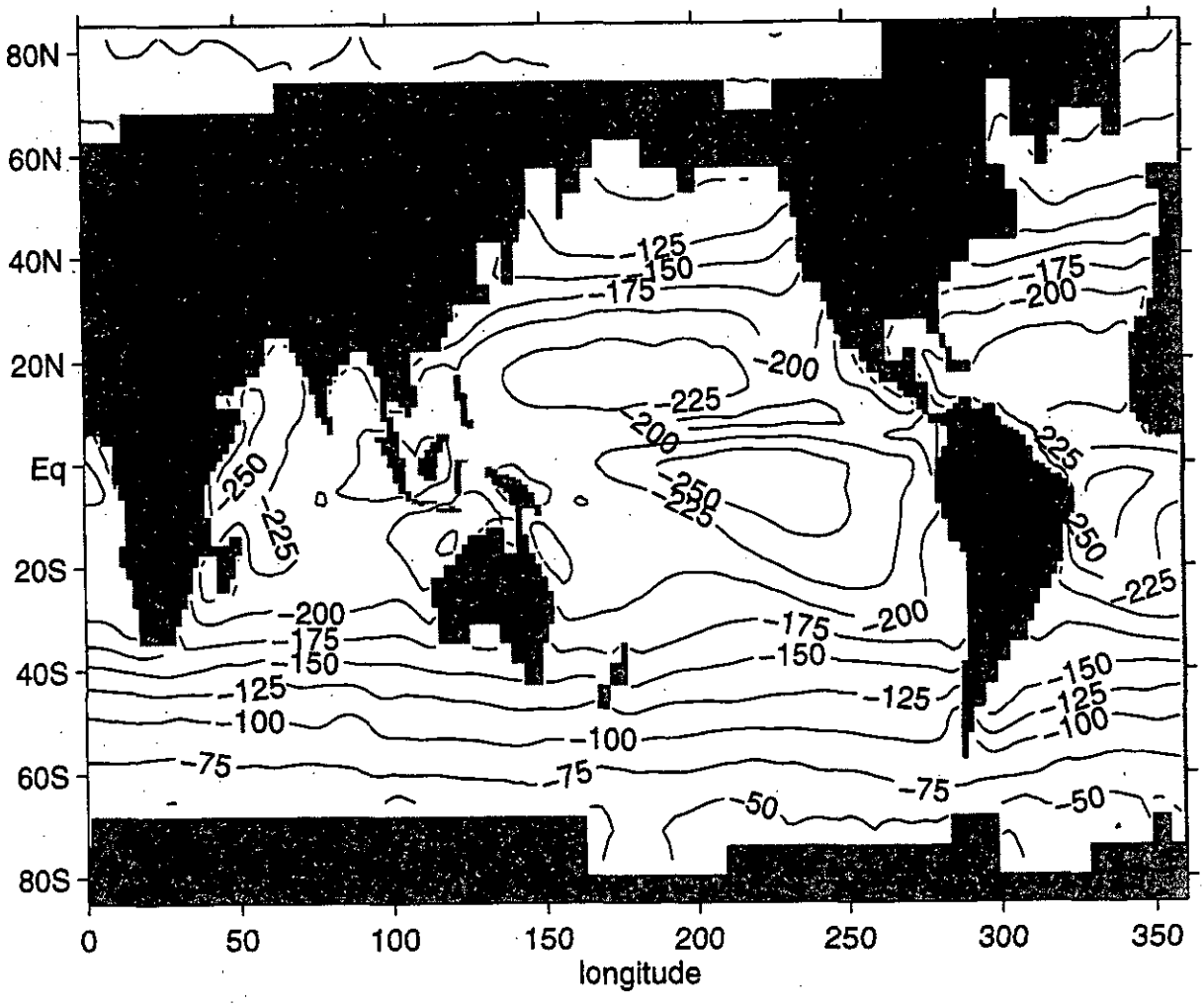

Figure 3.3a: ISCCP annual mean net shortwave radiation into the ocean (W/m^2).

Perhaps more importantly for Australian climate prediction purposes, the latent heat fluxes of Figure 3.4a are consistently too low in the southern subtropics (20°–40°S). The two effects that shortwave radiation is too strong, and that latent heat loss is too weak, cause $Q_{correct}$ to be more than $50\,W/m^2$ throughout the southern subtropics in Figure 3.2a.

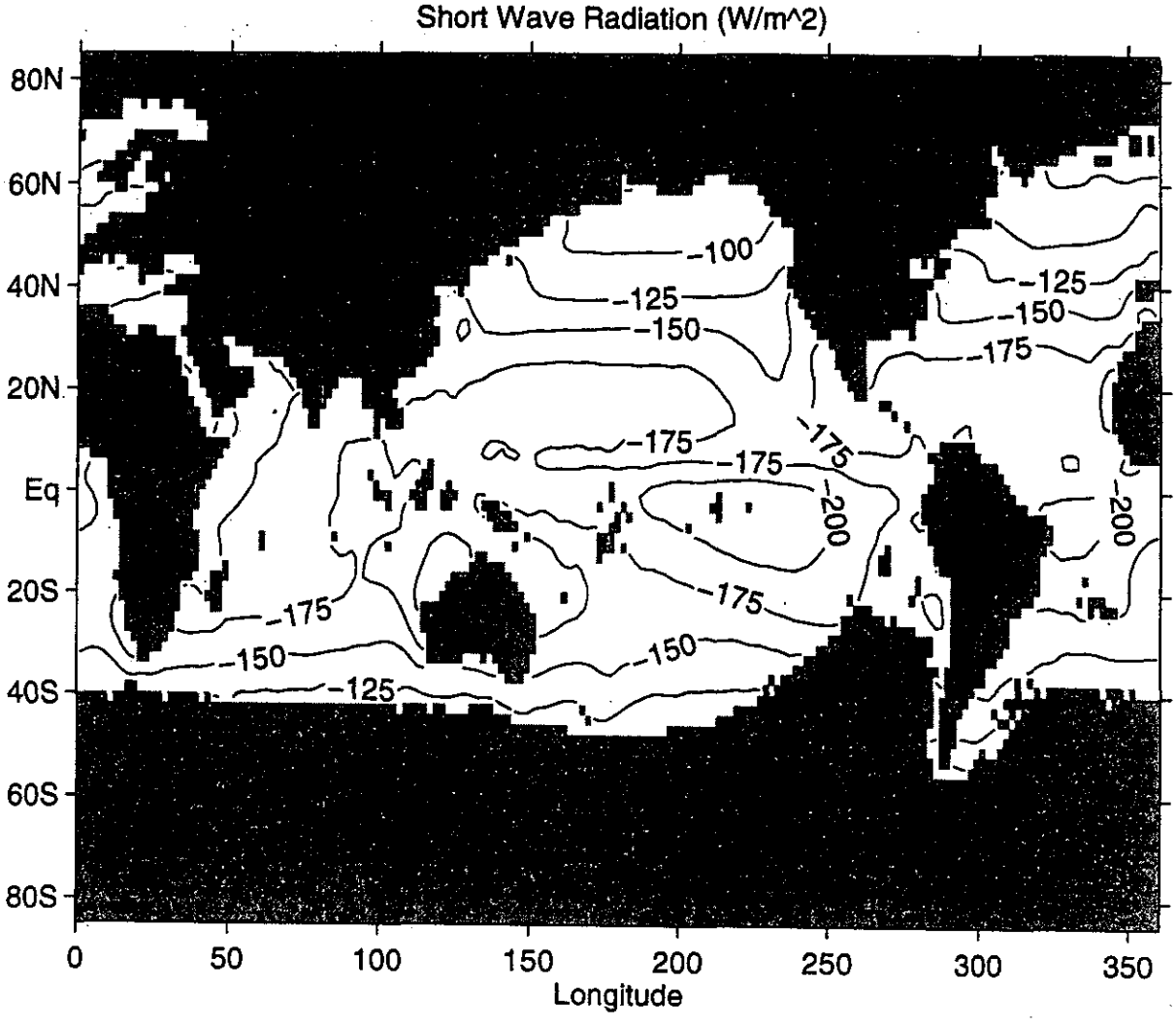

Figure 3.3b: Annual mean net shortwave radiation into the ocean from Oberhuber (1988), in (W/m^2).

Finally the sum of longwave and sensible heat loss from the third term on the right of (3.1) is quite accurate in the tropics, but omits peaks of up to 40 W/m^2 in the Kuroshio and Gulf Stream seen in Oberhuber and other climatologies.

In principle, the problems with the latent and sensible heat losses could probably be improved substantially by using the Kleeman and Power (1995) model of the Marine Atmospheric Boundary Layer. The problems with the shortwave radiation seem harder to correct; they are believed to be due to inadequacies in the radiative models used to infer surface shortwave radiation from satellite reflectance (J. Garratt, pers. comm.) However, for the present we are proceeding with runs to test our model's ability to generate realistic SST anomalies, despite these problems.

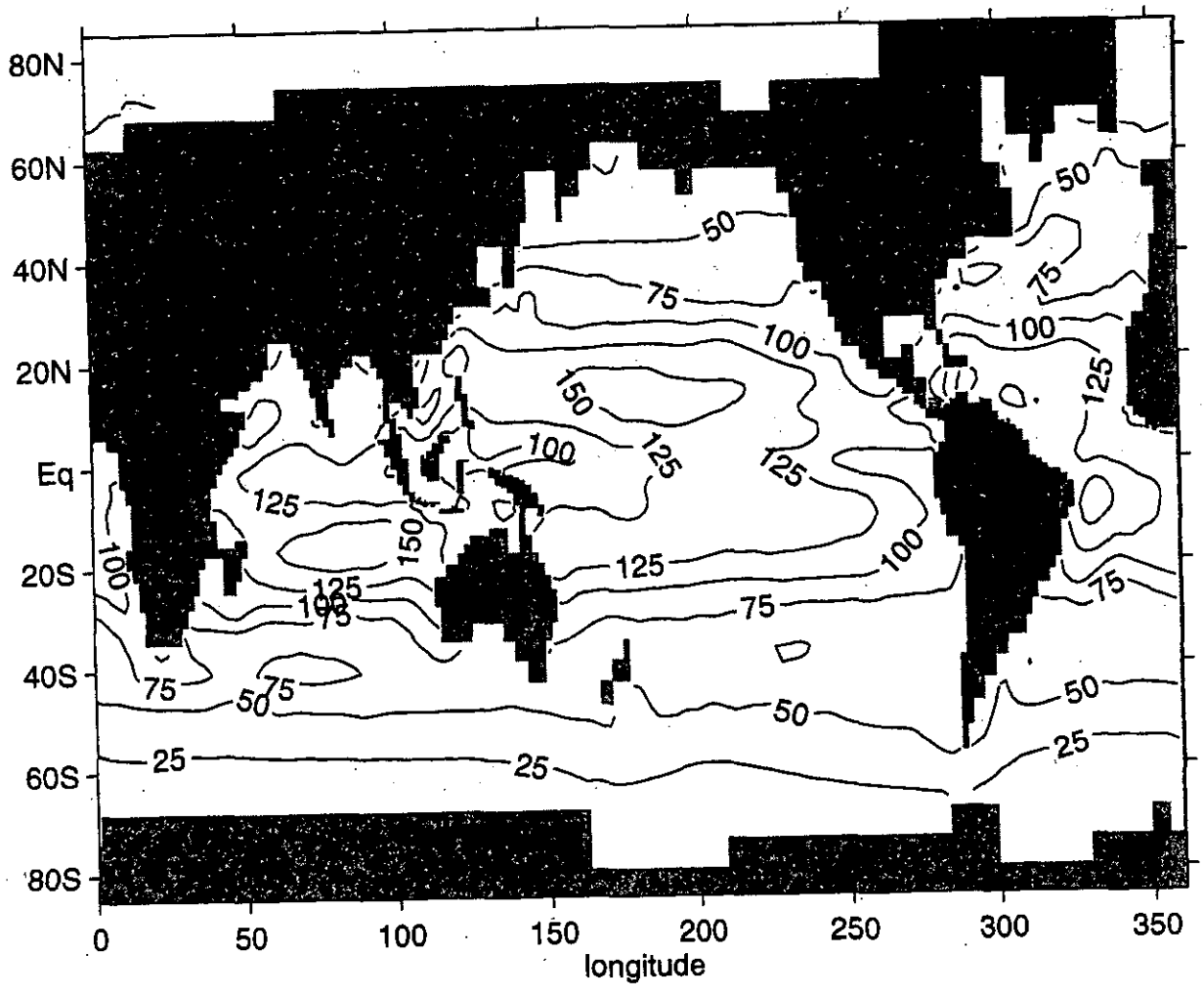

Figure 3.4a: Latent heat flux, estimated from the second term on the left of Eqn. (3.1), in W/r

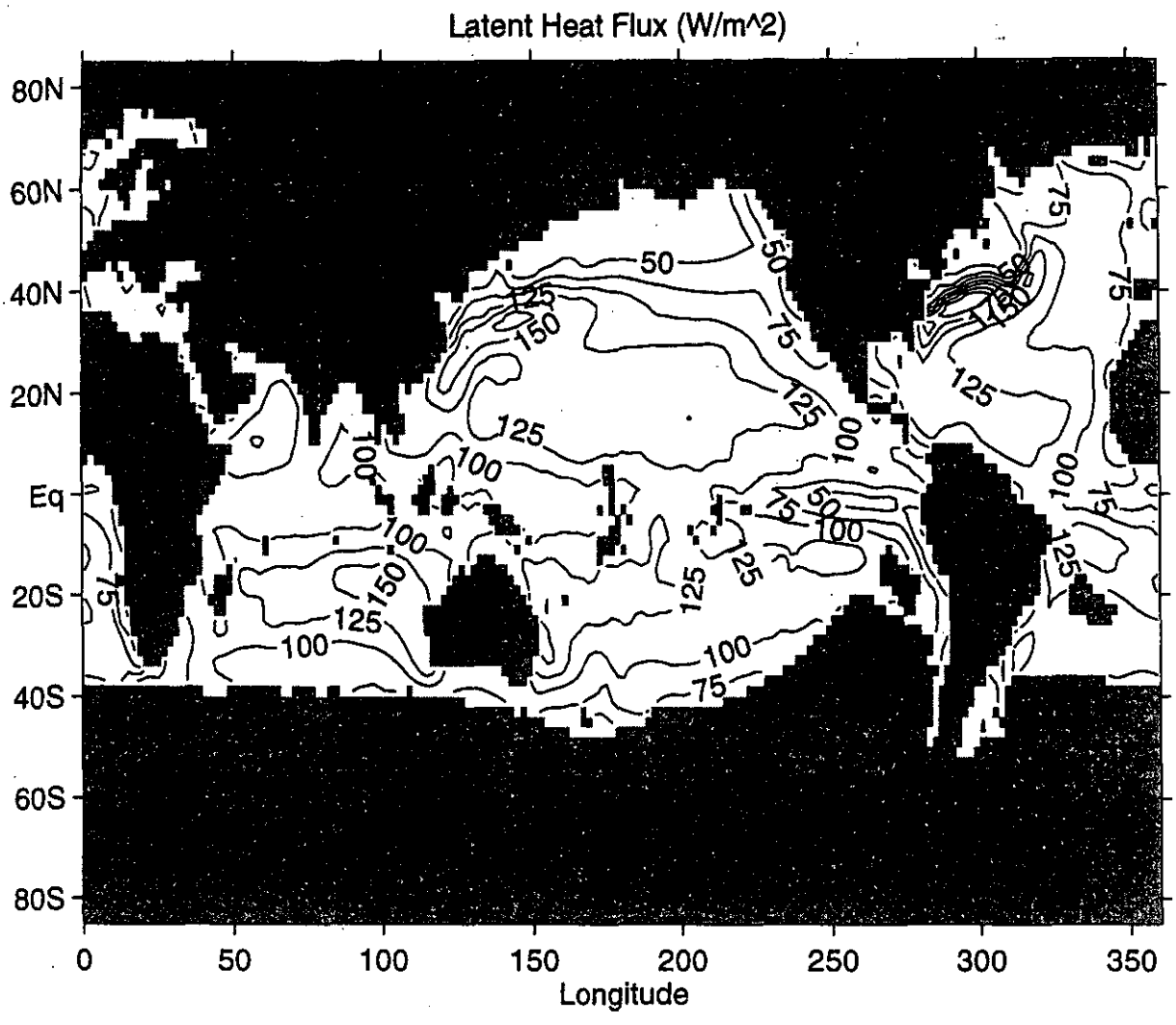

Figure 3.4b: Annual mean latent heat flux from Oberhuber (1988), in (W/m^2).

4 Mixed-layer depth

There are two immediate problems with comparing the model's mixed-layer depths with observations. The first is the definition of the mixed-layer depth itself, and the second is the scarcity of mixed-layer data.

We take as our definition the depth at which temperature falls by 1.0 °C from the surface value. In practice we use potential temperature, since this is what the model provides, but the difference is negligible. This definition is consistent with the data we have for comparison. A better definition would be based on density, since density is more closely related to stability of the water column. Sprintall and Tomczak (1992) point out that using a criterion based on temperature ignores salinity effects, which can lead to errors of typically 10–20 m, but up to 50 m, in determining mixed-layer depths in the tropics. Mixed-layer depths based on a density criterion were almost always shallower than those based on temperature alone.

Mixed-layer data are fairly scarce. Three sources of data are used here for comparison. Robinson (1976) gives depths to the top of the thermocline in the North Pacific based on bathythermograph data. The top of the thermocline is defined as that depth where the temperature is 1.1 °C lower than the surface value. Robinson et al. (1979) give the same data for the North Atlantic and northern Indian oceans. Wyrtki (1971) gives the two-monthly mixed-layer depth for the Indian Ocean, computed as an average of the 1.0 °C temperature-decrease criterion, and another criterion based on temperature gradient. Rao et al. (1989), using the 1.0 °C temperature-decrease criterion to define the mixed-layer depth, give monthly mixed-layer depths for the Indian Ocean.

One other option for obtaining mixed-layer data is to compute it from the Levitus and Boyer (1994) temperature data set. This was done for January in the Indian Ocean, and compared to the data from Rao et al. (1989) for the same month. The latter data is obtained by computing mixed-layer depths from each cast, and then averaging them. The computation from Levitus and Boyer does the calculations in the reverse order. This is evident when comparing the results: the Levitus–Boyer mixed-layer depths are less variable in space, with values that are less extreme by about 20 m. Hence we have decided to compare mainly with the Rao et al. (1989) data, concentrating on the months of February and August.

There is broad agreement between Rao et al. (1989), Wyrtki (1971) and Robinson et al. (1979). The following discussion uses the most recent data from Rao et al. (1989). The observed February mixed-layer depth (MLD) is greatest in the northern Arabian Sea, central Bay of Bengal, around the southern tip of India and off the coast of Sumatra, with values between 80 m and 100 m (Fig. 4.1a). There are values up to about 80 m along the

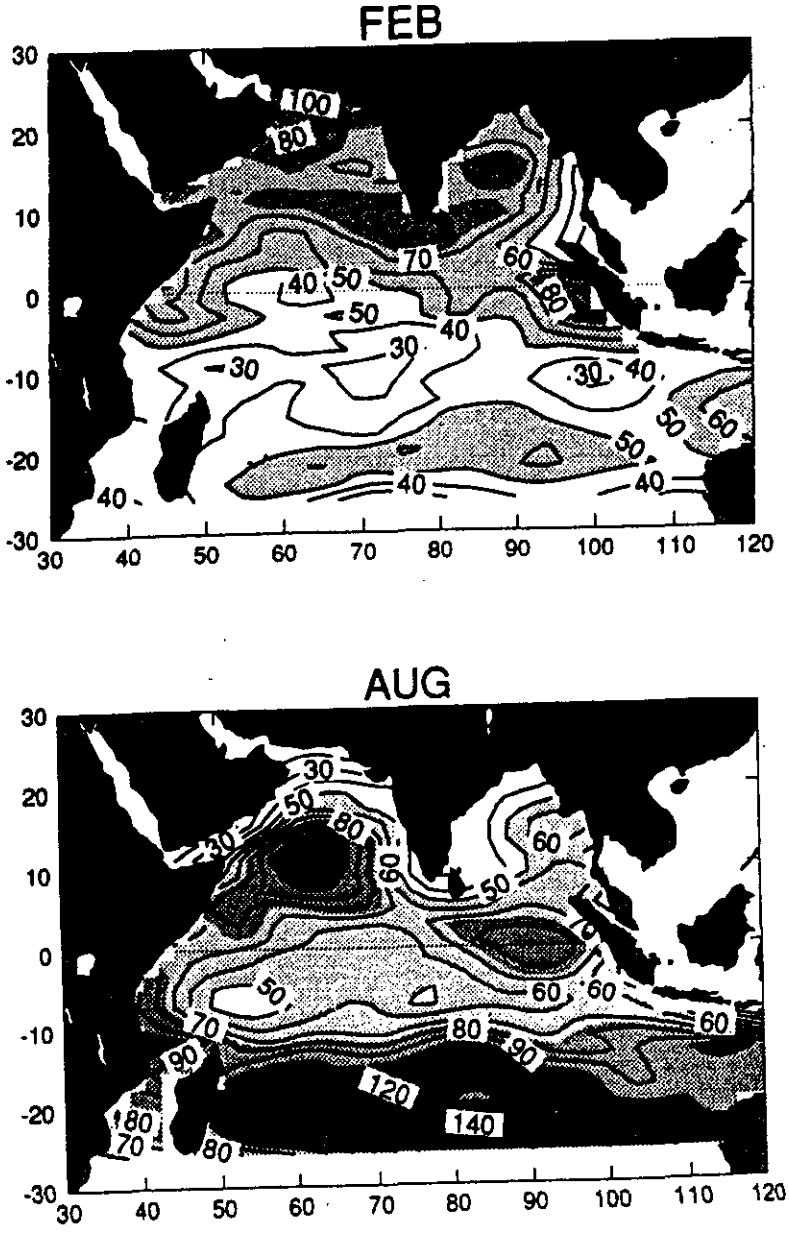

Figure 4.1: Observed mixed-layer depth (m) in the Indian Ocean (Rao et al. 1989): (a) February, (b) August.

Somali coast. The model (see Fig. 4.2) is in close agreement with these values, tending to be perhaps 10–20 m too deep in the Bay of Bengal, along the Somali coast. and to the west of Sri Lanka. The observations show minimum values of 30–40 m in a dipole pattern on the equator at 60°E and at 10°S, 70°E. The model reproduces this pattern, but is about 10 m too deep. Another minimum in the observations is at 10°S and 100°E, with a value of 30 m. The model has a minimum here too, but of 60 m. South of 10°S, the MLD values increase to a maximum of about 60 m at 20°S. The model behaves similarly, although the MLD tends to be a bit deeper in the eastern side of the basin up to 20 m greater than the observations. There is some evidence that the model is 10–20 m too deep south of 25°S, but the Rao data are sparse here.

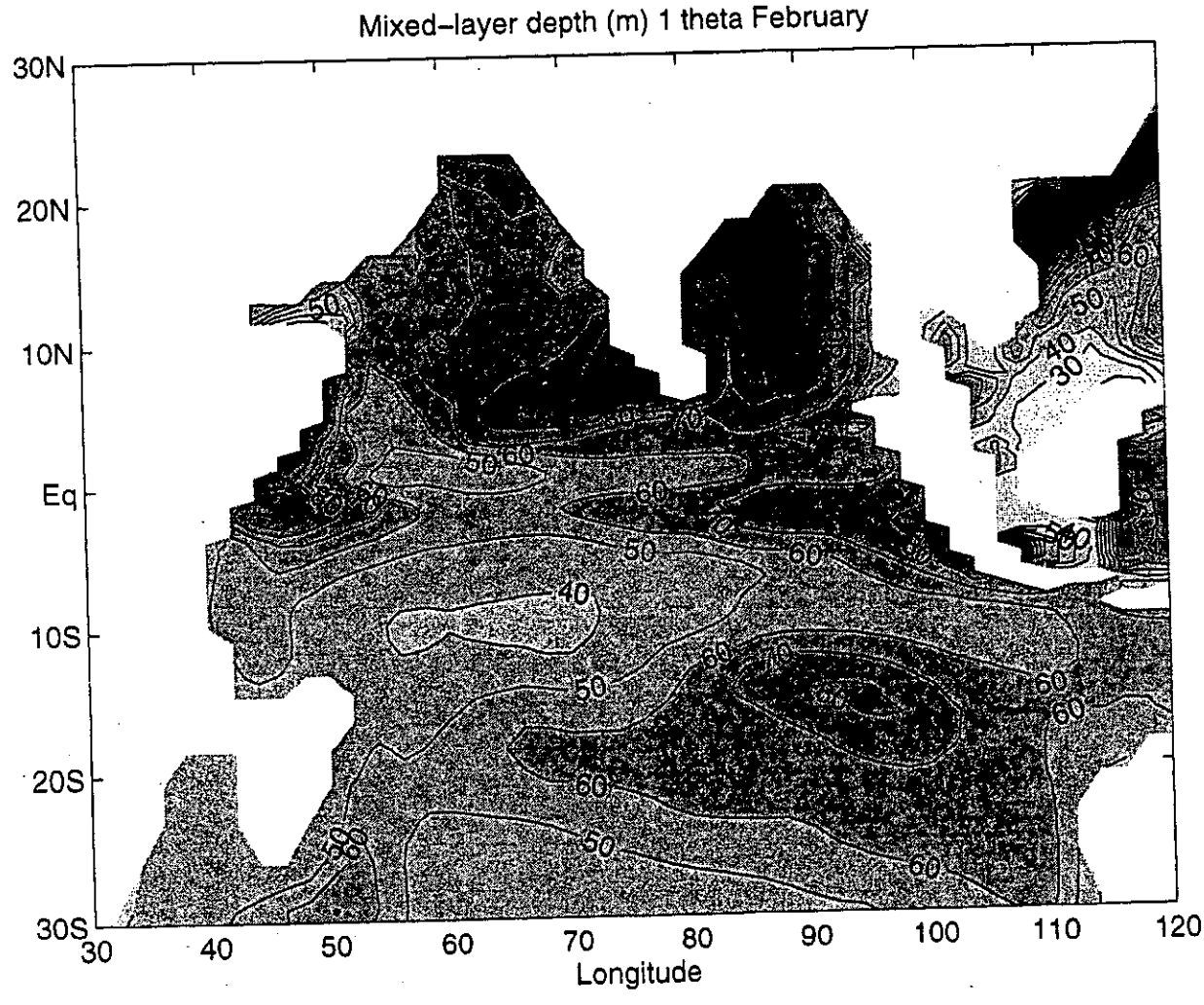

Figure 4.2: Model's mixed-layer depth (m) in the Indian Ocean for February.

The observed August MLD is now a minimum in the northern Arabian Sea and western Bay of Bengal, with values of 20–40 m (Fig. 4.1b). The model (see Fig. 4.3) is in good

agreement here. There is a maximum in the Rao data in the central south Arabian Sea, which the other two climatologies tend to put a bit further west. The value is over 100 m. The model's maximum is further west than any of the data, seemingly associated with the western boundary current, and with a depth of up to 140 m. Elsewhere, the model and Rao's data agree very well.

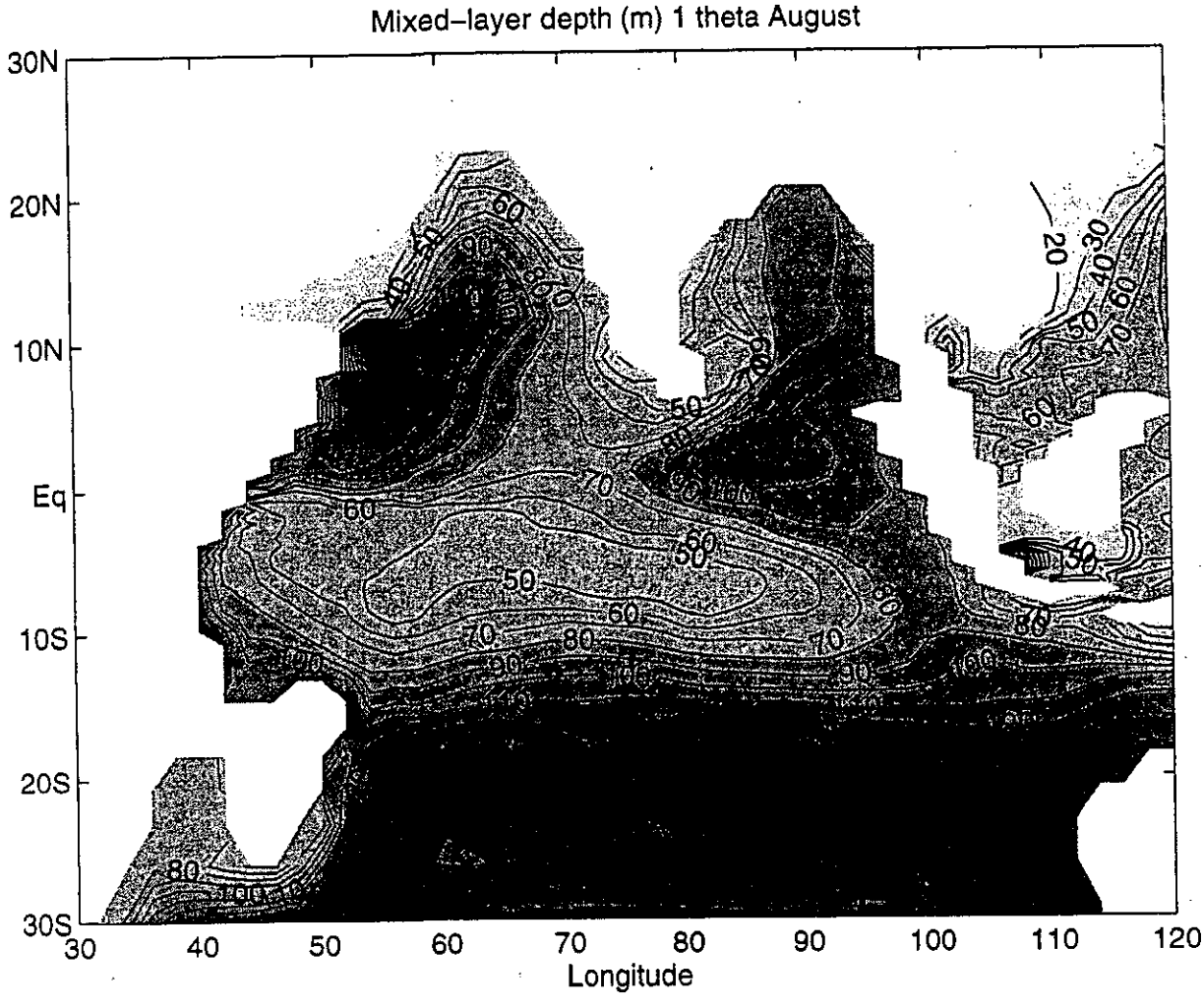

Figure 4.3: Model's mixed-layer depth (m) in the Indian Ocean for August.

The only other comparison that can be easily made is with the North Pacific data of Robinson (1976). In February, the data show maxima above 120 m at 30°N, 220°E; 15°N extending from 145°E to 190°E; and just south of the equator at 190°E (not shown). The model (see Fig. 4.4) captures these features, but tends to be a bit deeper at around 160 m. The broad patch of deep mixed layers at 15°N in the observations is about 5 degrees further north in the model (Fig. 4.4). The data show a large area in the eastern Pacific near the equator with shallows of around 15–30 m. The model has MLD values that

are roughly double this. In the western equatorial Pacific, the data show MLD values of 45–60 m. The model is again too deep, generally by about 30 m. The spatial patterns are generally quite similar everywhere.

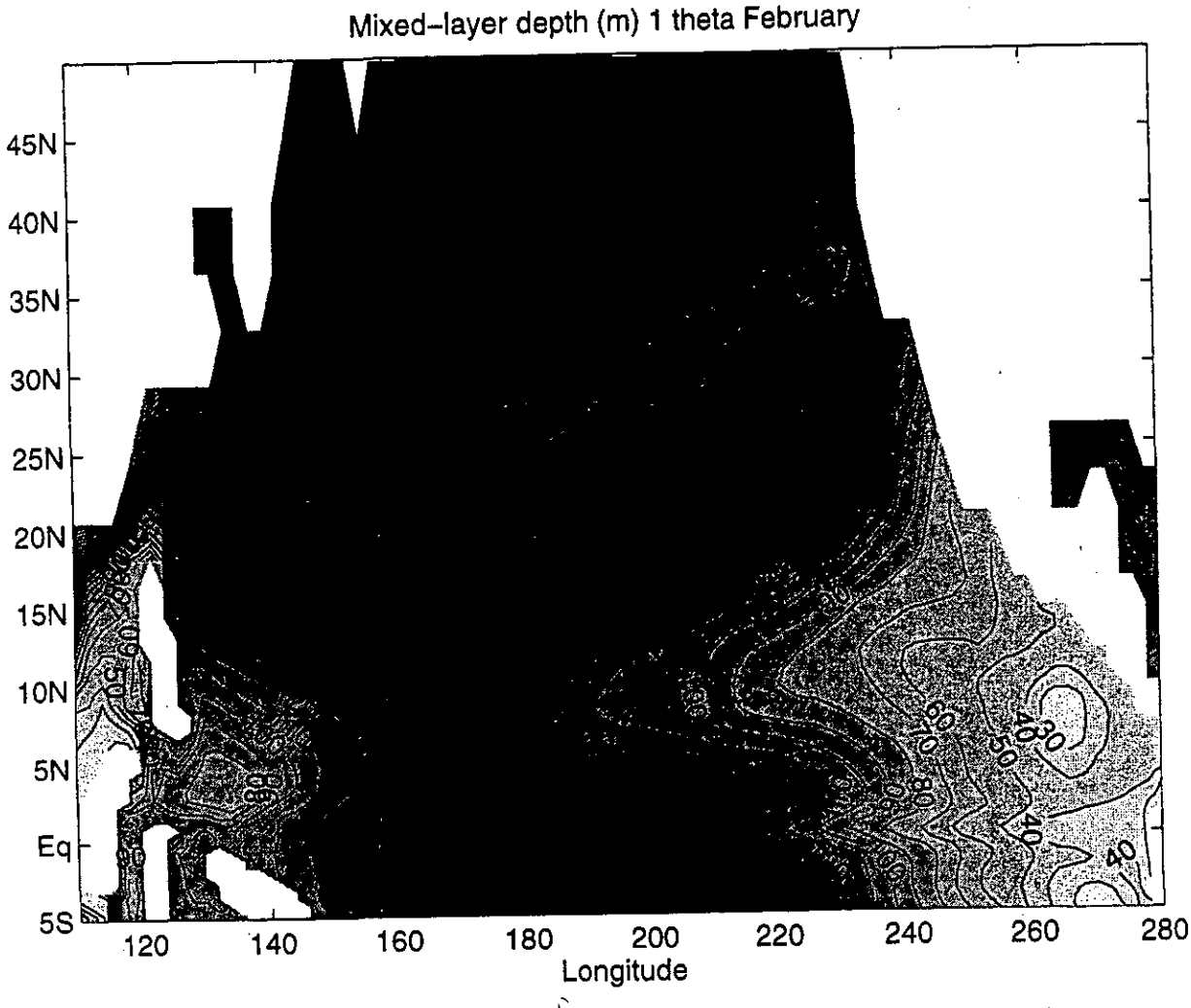

Figure 4.4: Model's mixed-layer depth (m) in the North Pacific Ocean for February.

In August, the whole Pacific north of about 30°N has mixed-layer depths of about 15 m (not shown). The model's values (see Fig. 4.5) are typically twice this. Just south of the equator at 190°E, the data indicate depths of more than 120m. which the model reproduces well. The data also show a dipole pattern in the central Pacific, with maxima of 75 m at 15°N, 205°E, and 105 m at 3°N, 195°E. The model has a similar dipole, but the depths are around 140 m, and the northern pole is shifted about 25 degrees to the west.

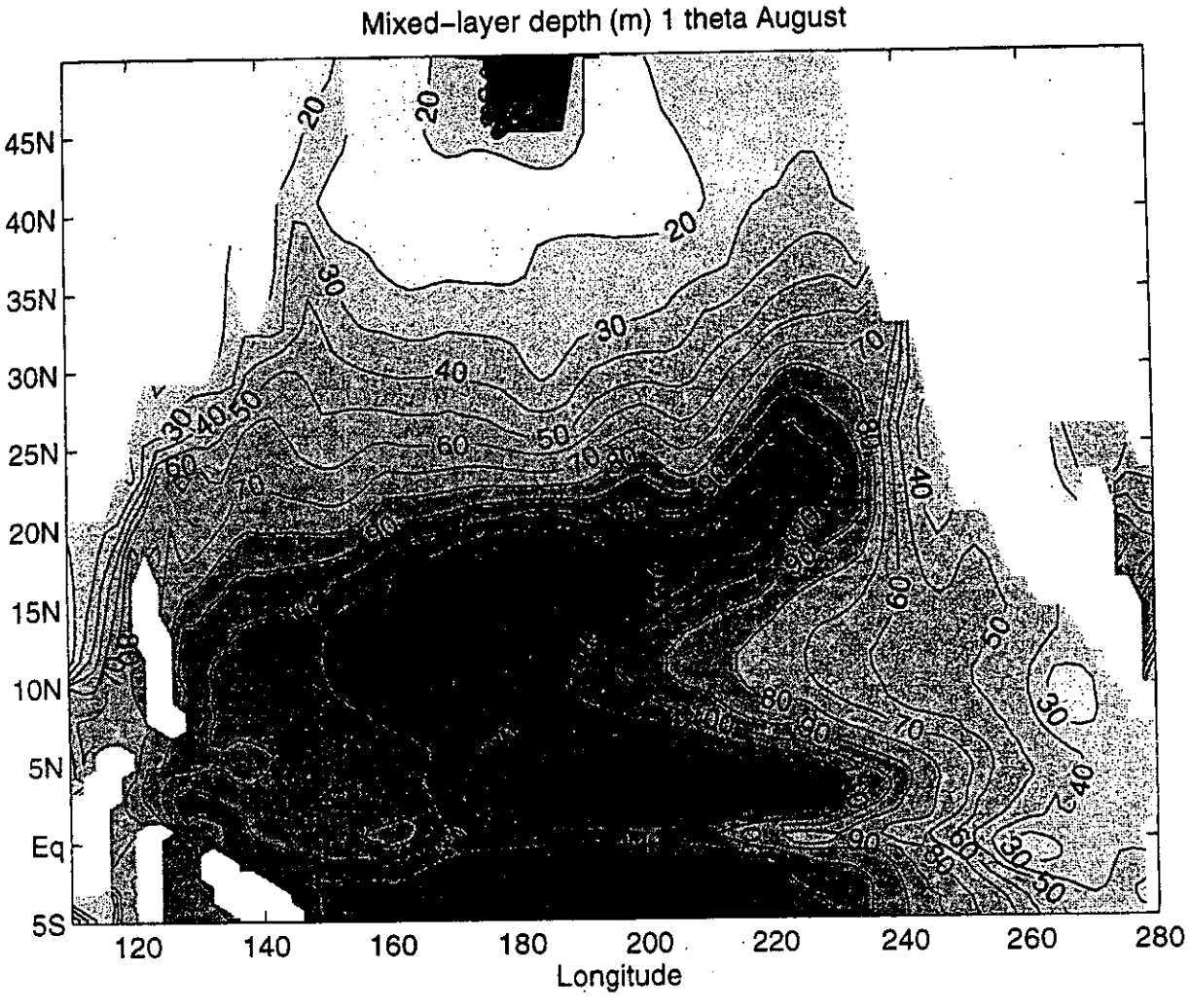

Figure 4.5: Model's mixed-layer depth (m) in the North Pacific Ocean for August.

To summarise, the model and data patterns of mixed-layer depth agree generally very well in the Indian and North Pacific ocean basins. There is a tendency for the model to have deeper mixed-layers than the observations, particularly in the North Pacific, where the model is too deep by 30–40 m.

5 Indonesian Throughflow

The most recent survey of measurements of the transport of Indonesian throughflow indicate a current that is highly variable, with a mean of 5–10 Sverdrups (Wijffels et al. 1996). Uncertainties in the mean arise from a lack of measurements of deep shear (the reference level used in geostrophic calculations) and relatively little data on salinity variation. Routine XBT measurements during 13 years indicate that most of the throughflow enters the region through Makassar Strait (Fig. 5.1), then flows eastward across the Flores and Banda Seas to enter the Indian Ocean near Timor I. through Ombai Strait and Timor Passage (Cresswell et al. 1993; Meyers et al. 1995). Nevertheless, direct current-meter measurements during one year indicate that 2 Sverdrups entered the Indian Ocean through Lombok Strait, flowing directly southward from Makassar Strait (Murray and

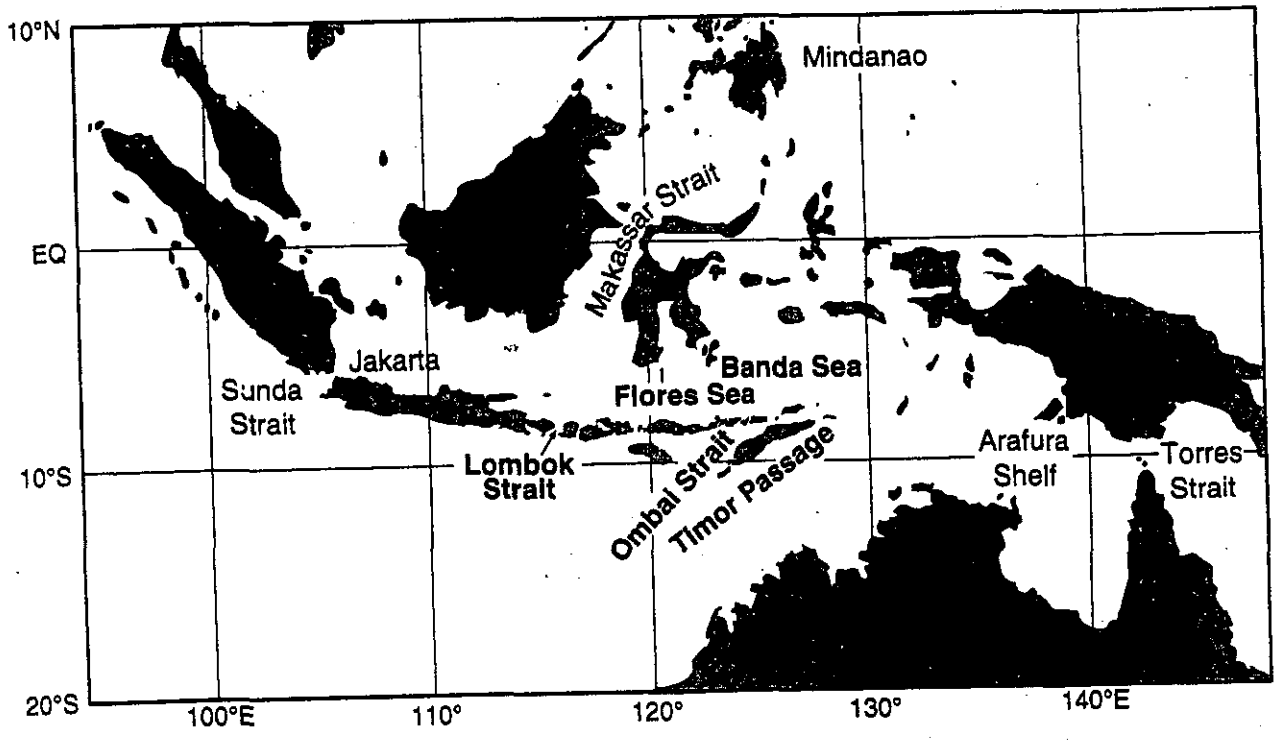

Figure 5.1: Map of the Indonesian Archipelago, showing the area of the throughflow.

Arief 1988). Although the measurements are far from definitive, we have assumed that a target for the model is to have 80% of the flow entering the Indian Ocean near Timor.

A high cross-strait dissipation was built into the Lombok Strait of the model to simulate the observed bifurcation of transports. By trial and error, the dissipation in Lombok Strait was increased to eight times the dissipation in the rest of the model's domain. The resulting annual mean barotropic stream function (Fig. 5.2) closely approximates the target defined above. However, the mean transport in the model is 16.5 Sv. This is high relative to the observations summarised by Wijffels et al. (1996), but is close to the Island Rule value, as often found in numerical models (e.g. Godfrey 1996).

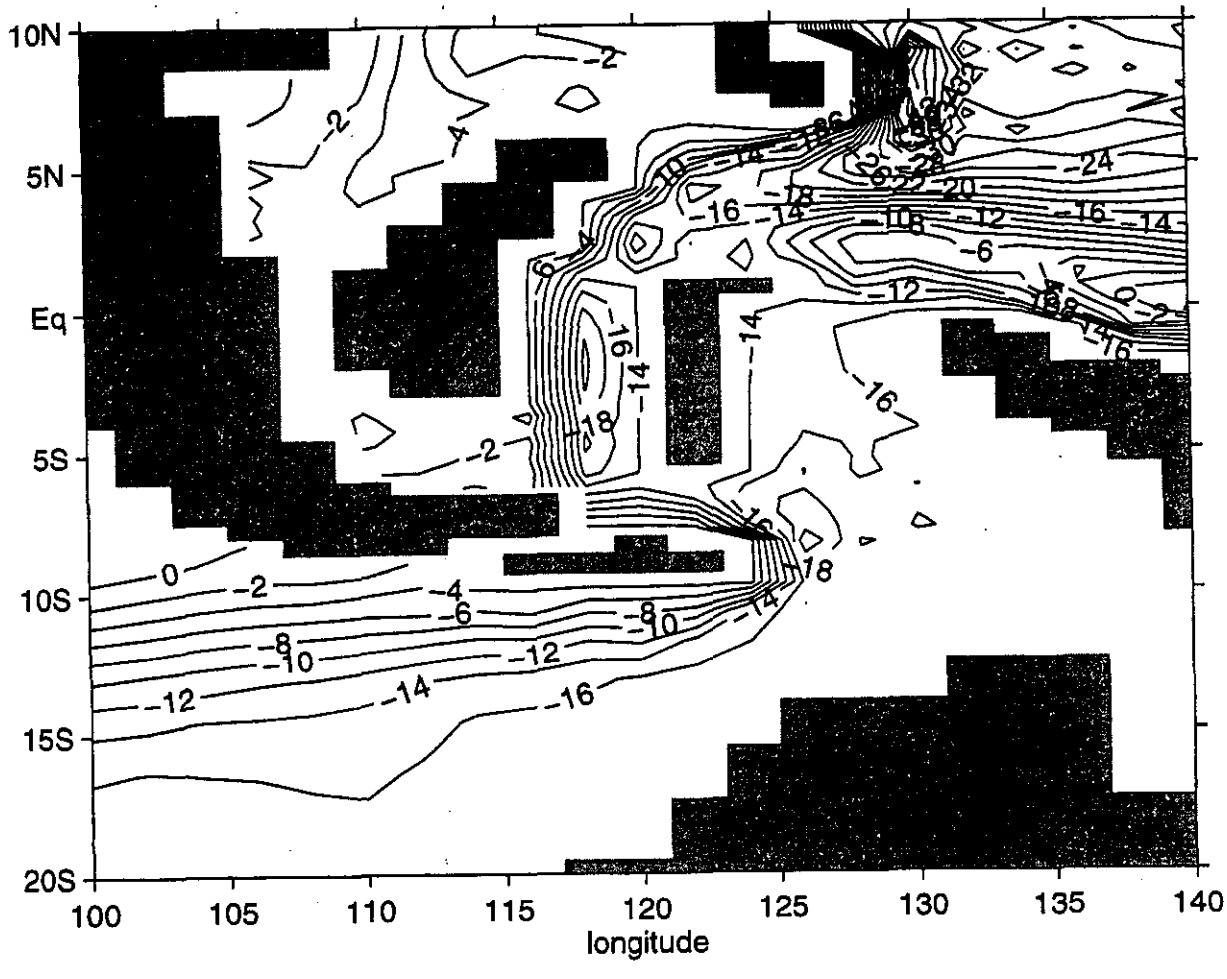

Figure 5.2: Annual mean barotropic stream function ($10^6\,m^3/s$) for Indonesian throughflow region.

The seasonal cycle of transports in the model (Fig. 5.3) has a maximum in October, a minimum in January–February and a seasonal range of 5 Sv. The maximum is one month later in the year than the observed maximum in the eastern Indian Ocean (Meyers et al. 1995), while the minimum is three months earlier. The observations have a much stronger semiannual variation, and a larger annual range by a factor of two. The observations were made on a shipping line between Shark Bay and Sunda Strait, about 1000 km west of the Timor Sea. The differences may in part be due to the observations and the model not covering the same location. Also, the barotropic transport is not measured in the XBT measurements.

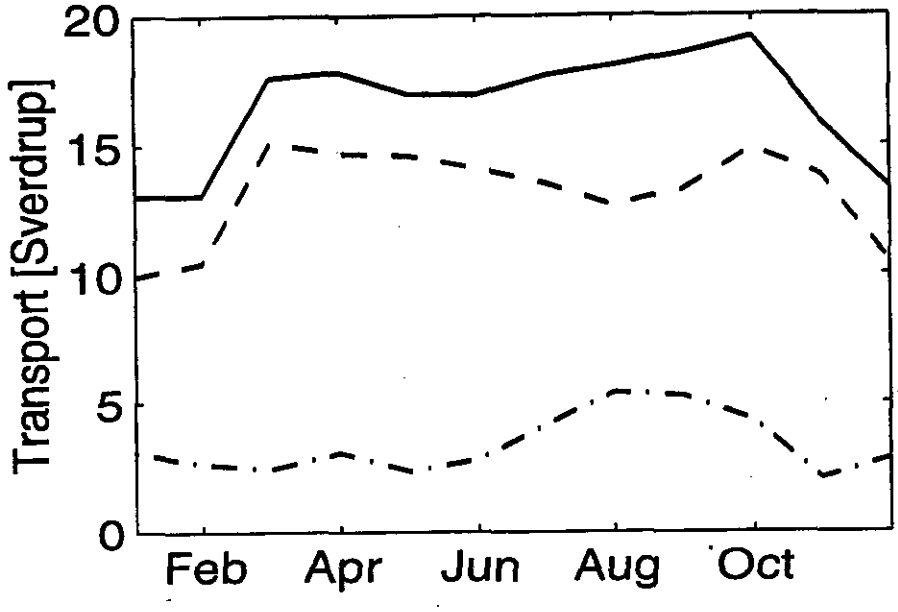

Figure 5.3: Seasonal cycle of Indonesian throughflow. Dashdotted: Lombok Strait, dashed: Timor Sea, solid: net throughflow. Units are in $10^6\,m^3/s$.

6 Structure of Equatorial Currents

The thermal structure and currents of the tropical oceans were observed better from 1985 to 1995 than ever before, due to the Tropical Oceans Global Atmosphere (TOGA) Program's observing system. The decade of observations provide an accurate description of the mean state and mean seasonal cycle of currents and thermal structure, particularly for the Pacific Ocean (McPhaden et al. 1996). A comparison of our model forced by wind stress and surface fluxes averaged over part of this period shows qualitatively similar structures on a large scale, with some important differences in detail.

The observed structure of the equatorial Pacific Ocean (Fig. 6.1b; McPhaden et al. 1996) shows the main thermocline (represented by the 20 °C isotherm) sloping downward from 40 m at 95°W off Ecuador to 160 m at 170°E, then slightly upward to 150 m at 143°E off Papua New Guinea. Associated with the topography of the thermocline is a rise in dynamic height of 42 dyn cm in the dynamic height 0/500 dbar (Fig. 6.1a). The model shows the 20 °C isotherm sloping downward from 50 m to 200 m (Fig. 6.2a) with a rise in dynamic height by 54 dyn cm (Fig. 6.2b). The observed wind stress has maximum easterlies of $0.055\,\mathrm{N/m^2}$ at 140°W, while the model's wind stress is approximately 36% stronger, with a maximum of $0.075\,\mathrm{N/m^2}$ at 150°W. The difference in wind stress is probably due to averaging the FSU wind product over 1985 to 1990, including a major La Niña event but not the El Niño events of the early 1990s. The steeper topography in the model may be due in part to differences in the field of wind stress (Fig. 6.2c). However, this slope is also dependent on eddy diffusivity, which is discussed in section 8.

The mean annual cycle of the depth of the thermocline and the zonal current (Fig. 6.3; McPhaden et al. 1996) has been described at four sites along the Pacific equator where temperature and current-meter moorings were maintained. Records were kept at these sites for different lengths of time from 3 to 11 years, which do not generally match the period over which the wind stress was averaged to drive the model. The interannual variation of the equatorial Pacific is strong and may affect the estimates of the observed mean seasonal cycle described below.

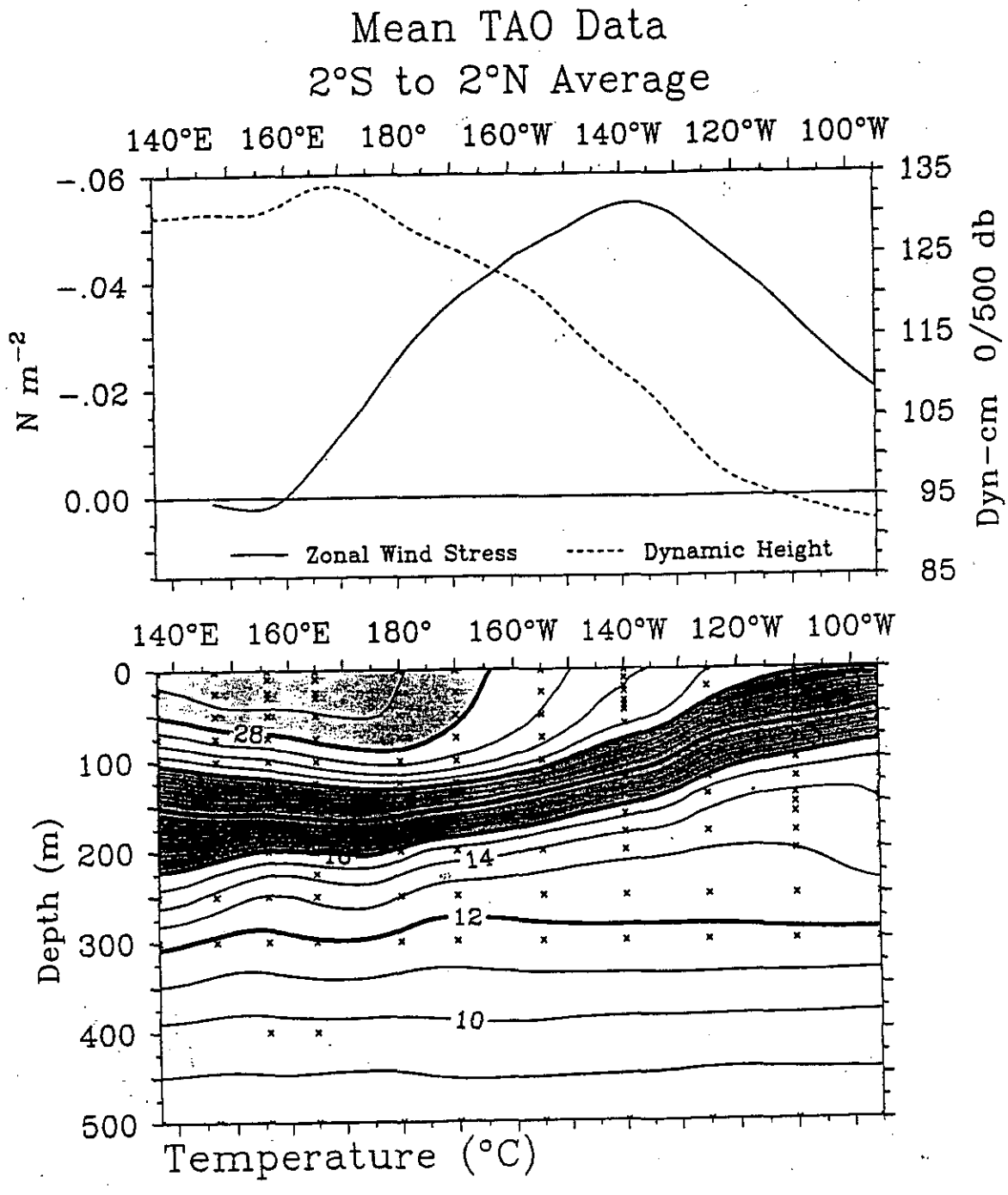

Figure 6.1: (a) Observed zonal wind stress and dynamic height; (b) temperature section of the equatorial Pacific averaged over 1985-1995 (from McPhaden et al. 1997).

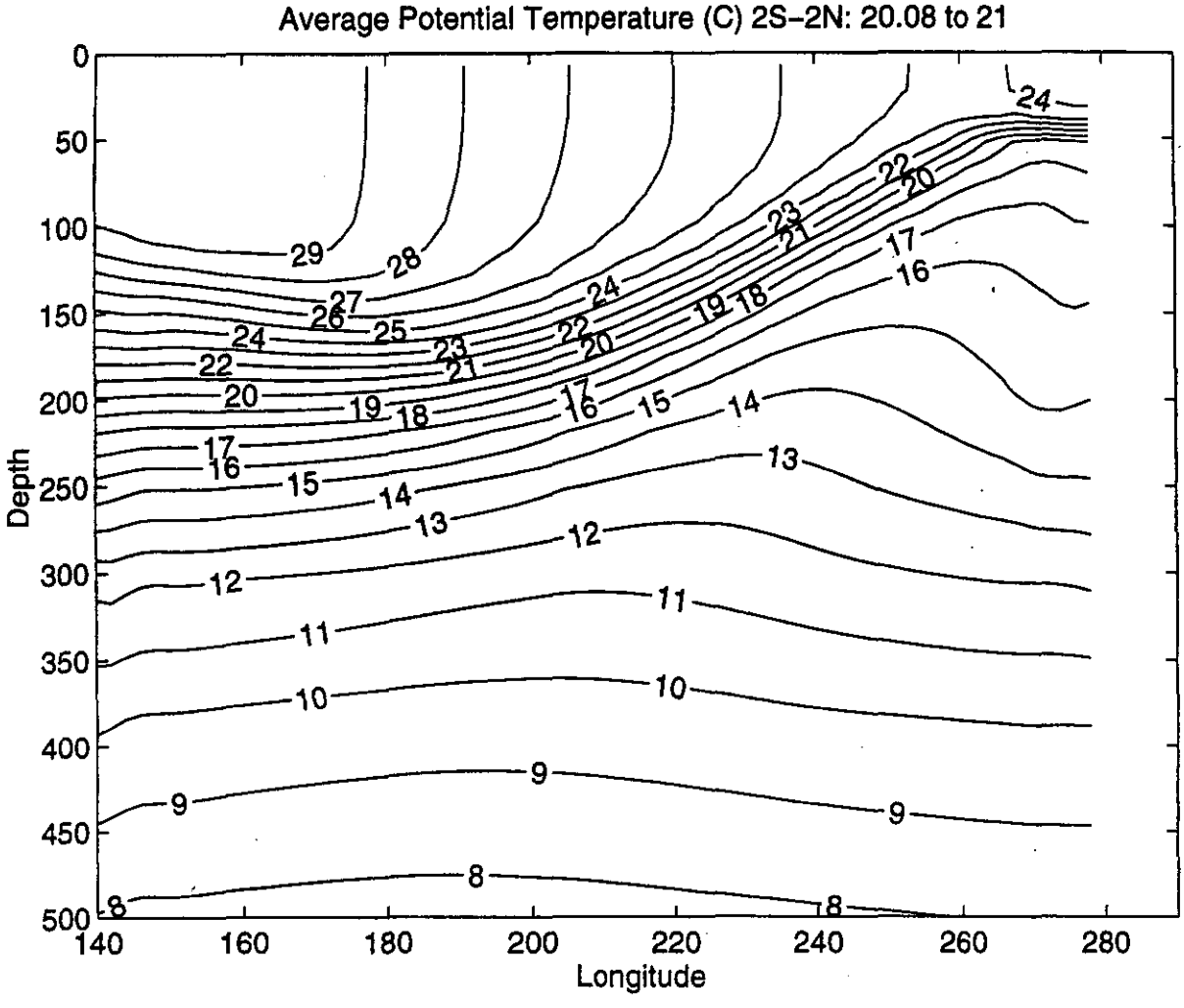

Figure 6.2a: The model's annual mean potential temperature (°C) along the equator.

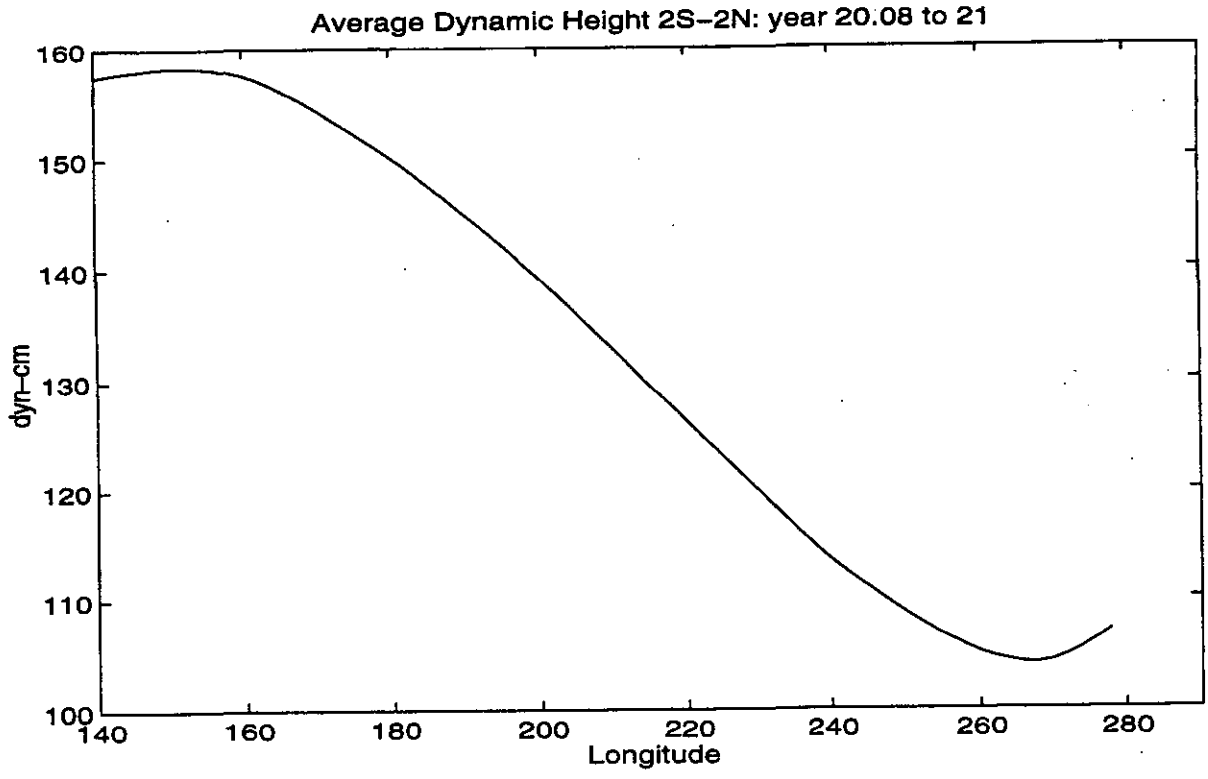

Figure 6.2b: The model's annual mean dynamic height (dyn cm) along the equator.

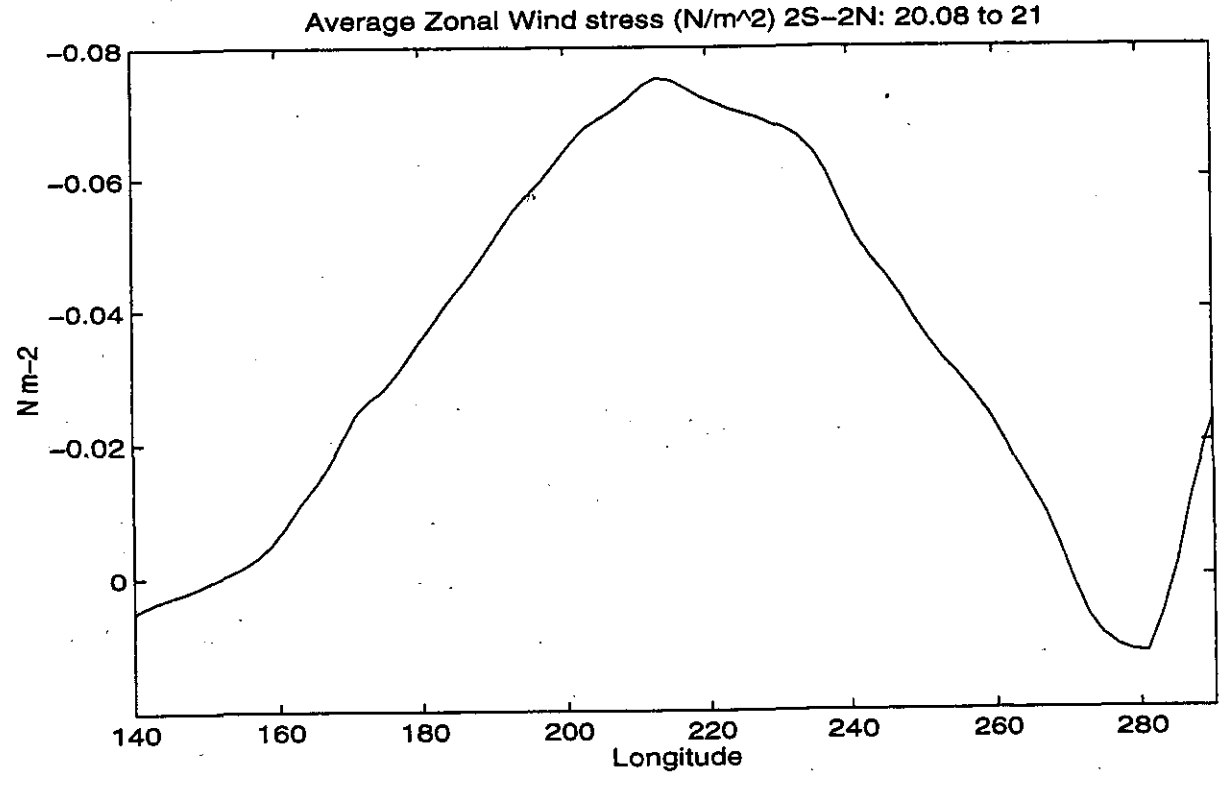

Figure 6.2c: The model's annual mean zonal wind stress N/m^2 along the equator.

The dominant feature of the equatorial Pacific (Fig. 6.3, McPhaden et al. 1997) is the Equatorial Undercurrent (EUC), flowing eastward near the depth of the 20 °C isotherm. The maximum velocity in the core of the EUC at a depth slightly less than 100 m is 120 cm/s at 140°W in the eastern central Pacific during April–May–June. The core velocity decreases toward the west to 40 cm/s at a deeper level and decreases to 100 cm/s toward the east at a shallower level. The model produces an EUC with maximum core-velocity of 100 cm/s at slightly more than 100 m depth near 140°W. The model's annual cycle and distribution of speed and depth toward the west matches the observations very well (Fig. 6.4). The surface currents are westward in both the observations and model; however the observed EUC surfaces for longer periods during the seasonal cycle than the model EUC. The observed annual variation in isotherm depths has a dominant annual cycle in the eastern Pacific and semiannual cycle in the western Pacific. The model produces a similar distribution of annual and semiannual cycles with about the right amplitude of vertical displacements.

The thermocline throughout the tropical Pacific — 30°N to 30°S — has a characteristic topography (Wyrtki and Kilonsky 1984; Delcroix et al. 1987), which is closely related to the broadscale Equatorial Current System. The westward South Equatorial Current (SEC) and return flow at higher latitude are indicated by a bowl in the thermocline (represented in Fig. 6.5 to 6.7 by 15 °C from Levitus and Boyer, 1994) that slopes downward to the west from 290 m at 110°W, to 360 m at 156°W, then is nearly flat to 370 m at 166°E (Figs. 6.5-6.7). The model also produces a bowl in the thermocline associated with the SEC; however it is flatter and the eastward shear below 150 m is not prominent. The depth of the 15 °C isotherm in the model at the three longitudes given above is, respectively, 280 m, 340 m and 350 m, tending to be shallower than the observations.

The westward North Equatorial Current (NEC) is indicated by a similar bowl in the thermocline. The observed depth of the 15 °C isotherm 110°W, 156°W and 166°E is 115 m, 250 m and 300 m; the model's depth is 150 m, 270 m, 355 m. The model's NEC bowl is therefore deeper than observations, while its SEC bowl is shallower. The differences again may be due to differences in details of the wind field during the five-year averaging period 1985–1990. A thermostad of 16 °C water (Masuzawa 1969) appears in the observations but is not produced in the model.

The North Equatorial Countercurrent (NECC) is indicated by a trough and ridge in the thermocline between the equator and 10°N. The structure is produced by the model; however, the eastward shear of the NECC is weaker than the observations, especially in the deeper part of the thermocline below 15 °C.

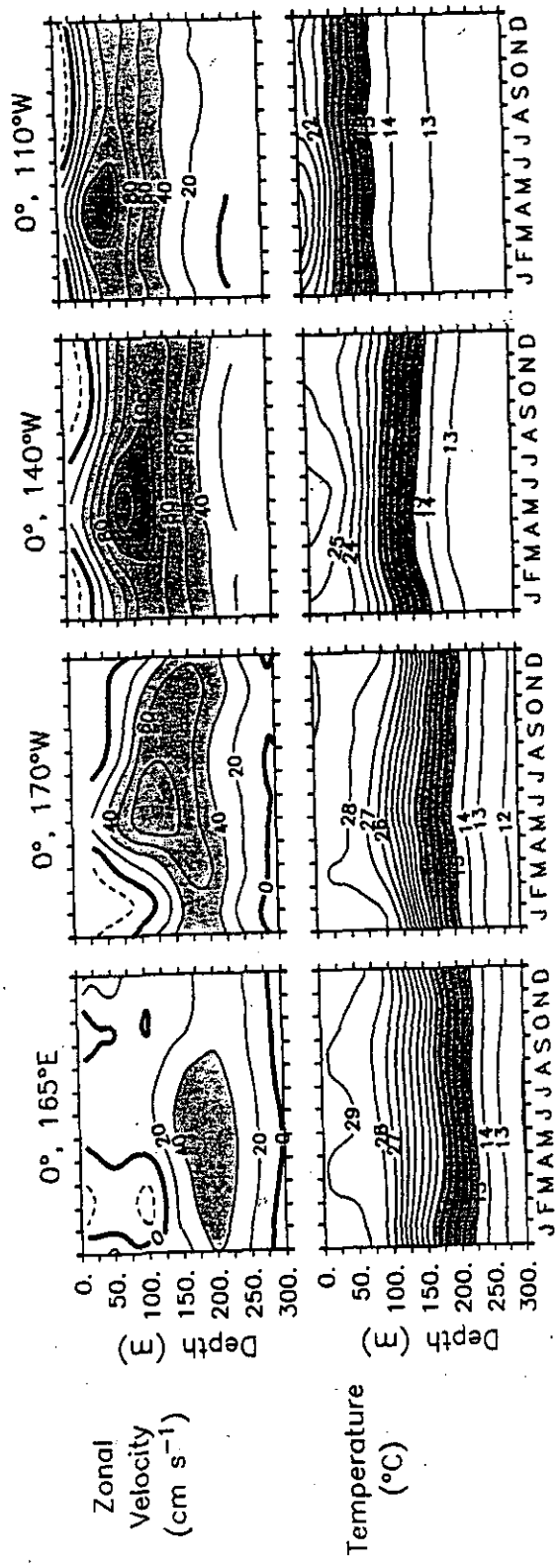

Figure 6.3: Observed annual cycle of (a) zonal velocity and (b) temperature at four sites in the equatorial Pacific (McPhaden et al., 1996).

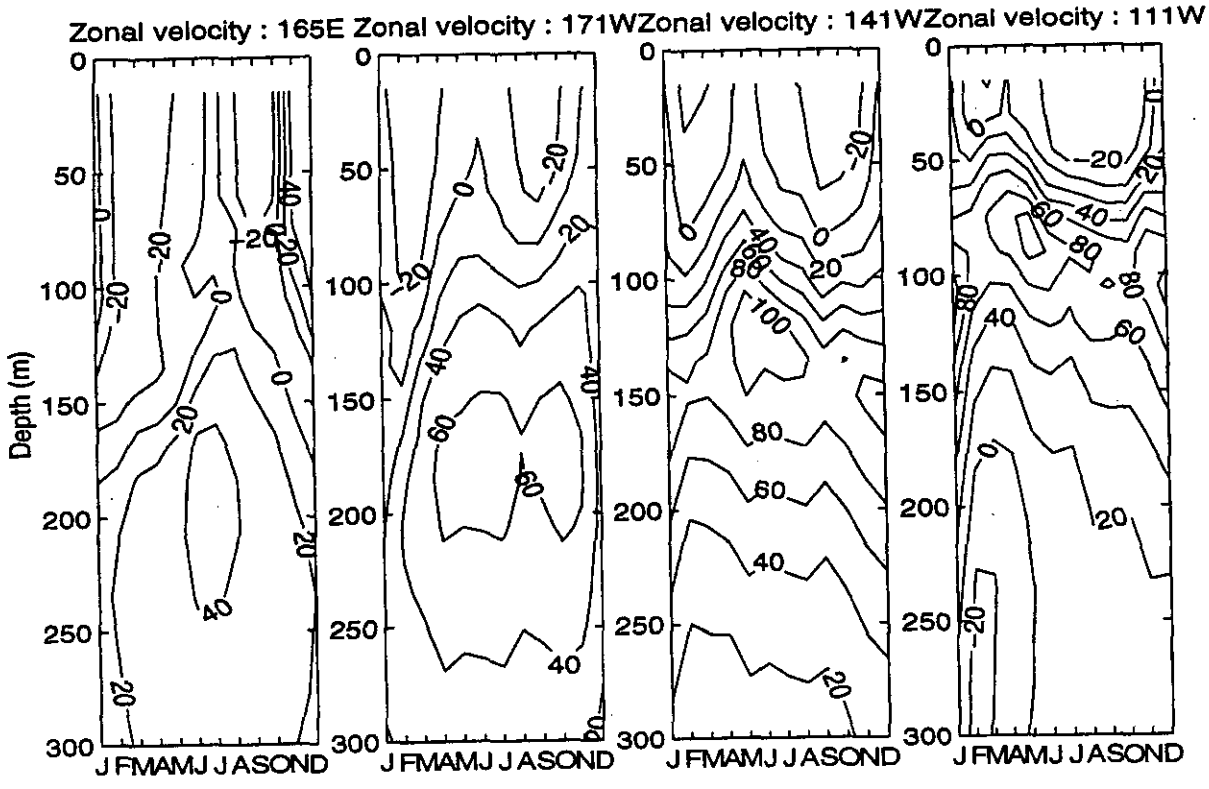

Figure 6.4a: Model: annual cycle of zonal velocity (cm/s) at four sites in the equatorial Pacific from model.

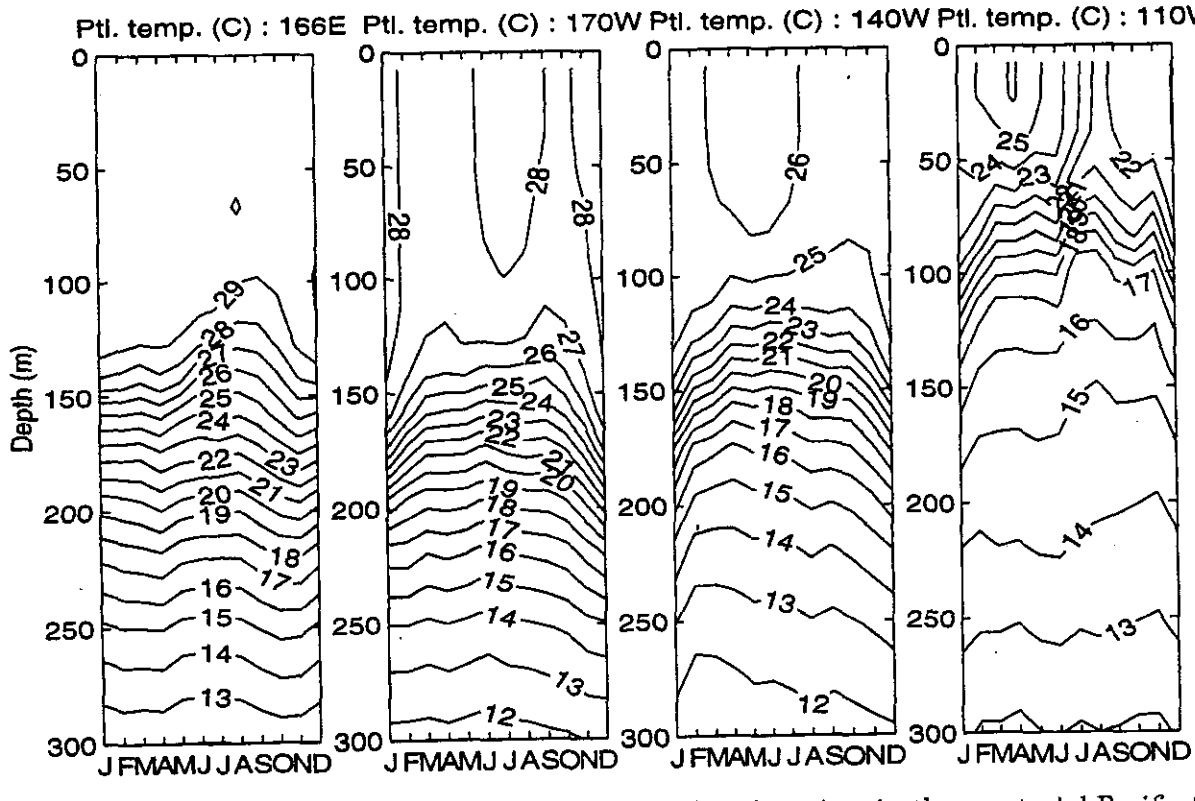

Figure 6.4b: Model: annual cycle of potential temperature (°C) at four sites in the equatorial Pacific from model.

The spreading of the thermocline at the equator associated with the EUC does not appear in the model in the western Pacific, but is evident in the central and eastern Pacific. It is worth noting that the observed spreading as represented in the climatological data of Levitus and Boyer (1994) is considerably smoothed in comparison to synoptic data. A quantitative comparison of the observed and modelled currents and transports near the equator is beyond the scope of this report. The qualitative differences in the ridge/trough structure and spreading of the thermocline call out for a quantitative comparison, including assessment of the model's capacity to influence SST by horizontal advection.

The observed structure of currents in the tropical Indian Ocean is limited to a few studies, based on a smaller quantity of data than from the Pacific (McPhaden 1982; Molinari et al. 1990; Hastenrath and Greischar 1991; Donguy and Meyers 1996). For a first attempt at qualitatively comparing the model to observations, we have used the most comprehensive measure of equatorial currents (McPhaden 1982) and the climatological temperature data of Levitus and Boyer (1994). As in the case of the Pacific, a quantitative comparison making full use of the available data is needed.

During the Gan I experiment at 73°E (McPhaden, 1982) the dominant signal in the equatorial current was a wind-driven, semiannual oscillation with a maximum, surface eastward current of 100 cm/s in May and November and a minimum, westward flow of 10 to 50 cm/s in July and February. The observations suggested this signal extends to a depth of 80 m with little damping. The model produces a similar current (Fig. 6.8), with maxima slightly less than 100 cm/s extending to 67.5 m. The observations did not distinctly show this signal at a depth of 160-180 m, while the model shows a distinct semiannual oscillation at 175.1 m. The upward propagation of phase in Figure 6.8 is indicative of downward propagation of energy due to wind-forcing at the surface (Luyten and Roemmich 1982).

The observed broadscale distribution of temperature (Figs. 6.9b and 6.10b) indicates a bowl in the thermocline associated with the SEC in the Indian Ocean. As with the SEC in the Pacific, the eastward shear below 200 m and poleward of 20°S is distinctive in the observations, but does not develop as clearly in the model (Fig. 6.9a and 6.10a). In the observations the depth of the 15 °C isotherm at the deepest part of the bowl slopes downward from 290 m at 110°E in the Indian Ocean to 330 m at 56°E (Fig. 6.9b, 6.10b). In the model the westward slope is greater, going from 300 m at 110°E, 20°S to 430 m at the same latitude at 56°E (Fig. 6.9a, 6.10a).

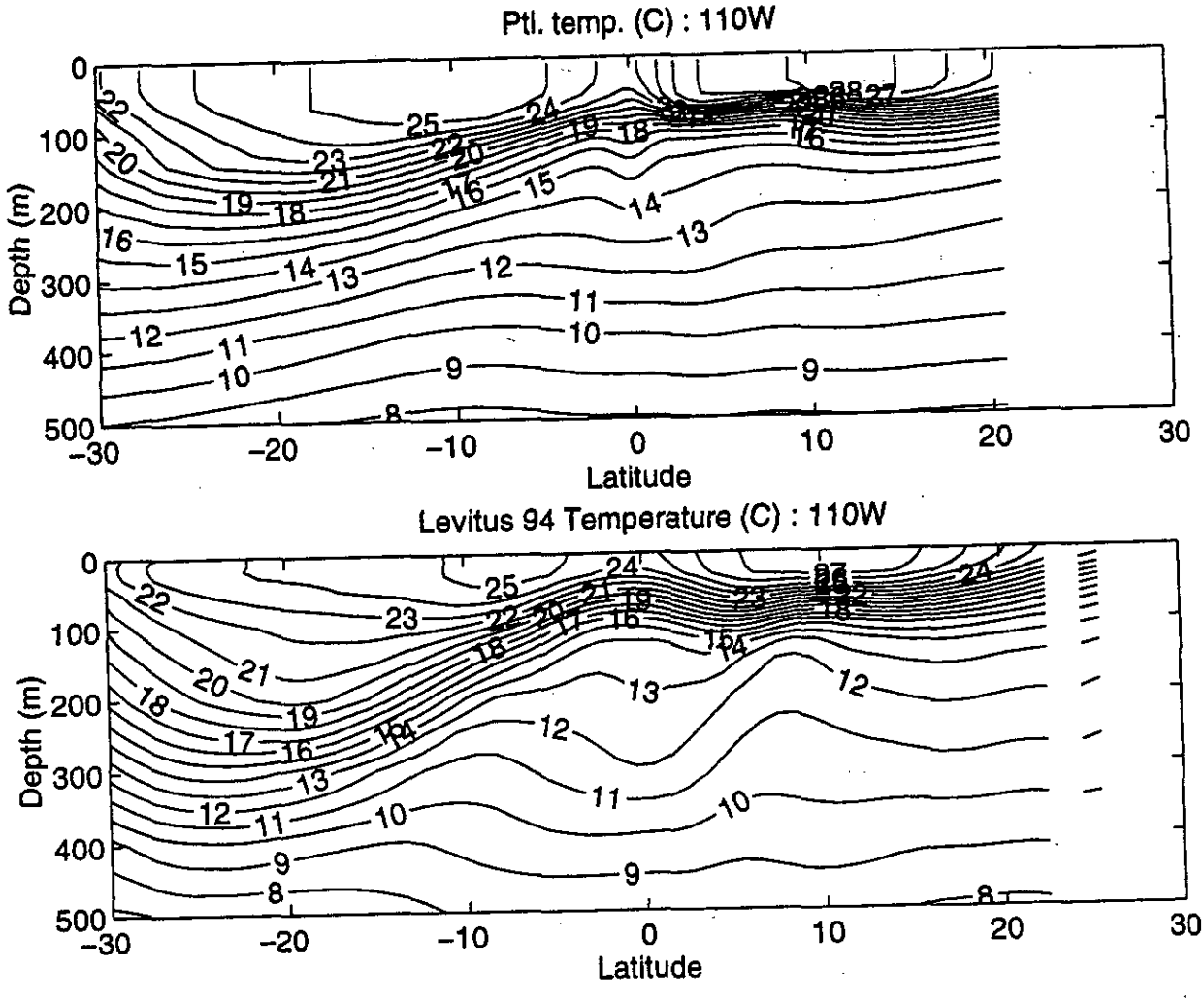

Figure 6.5: Annual mean potential temperature (°C) section along 110°W, (a) in model and (b) from Levitus and Boyer (1994).

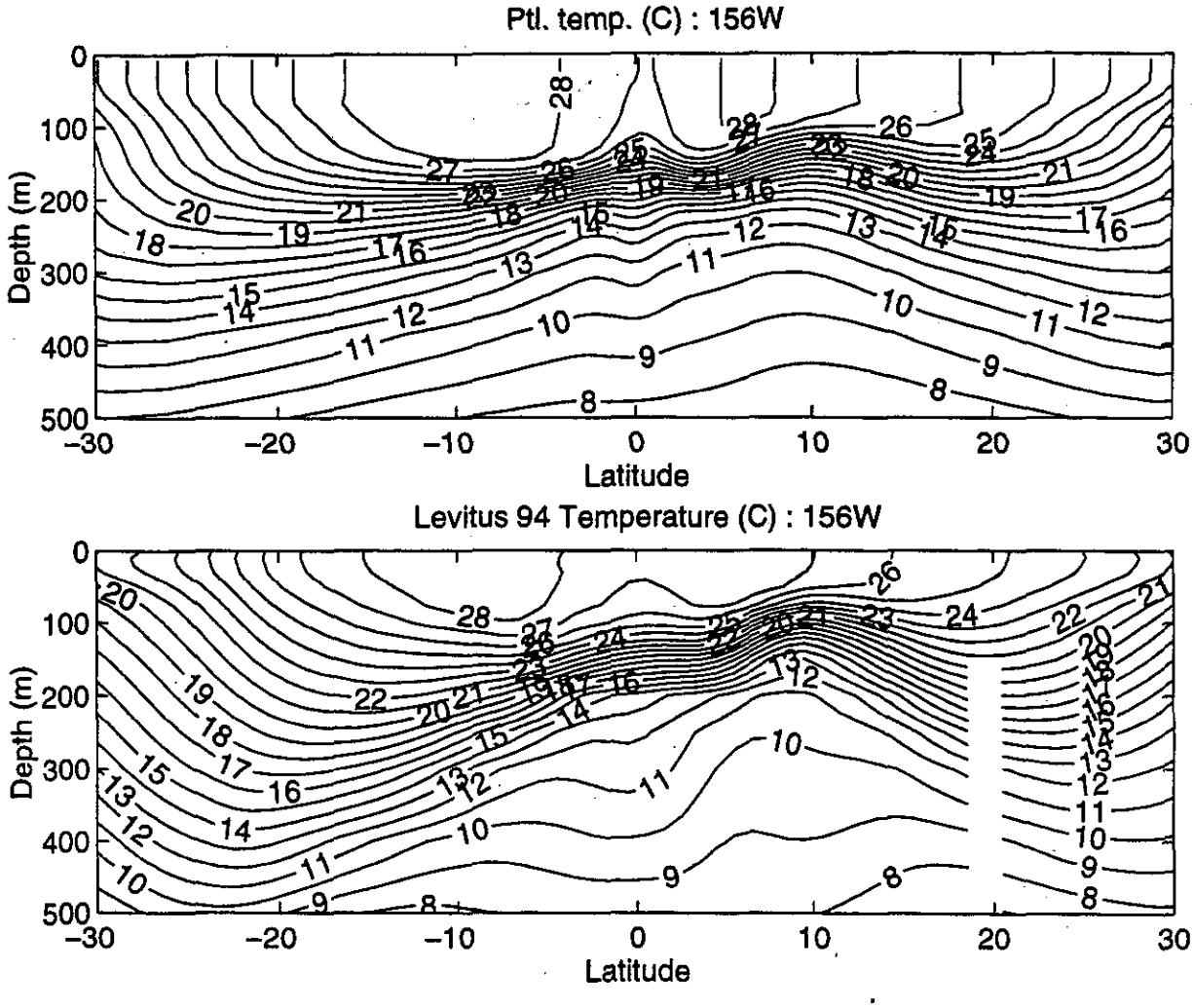

Figure 6.6: Annual mean potential temperature (°C) section along 156°W, (a) in model and (b) from Levitus and Boyer (1994).

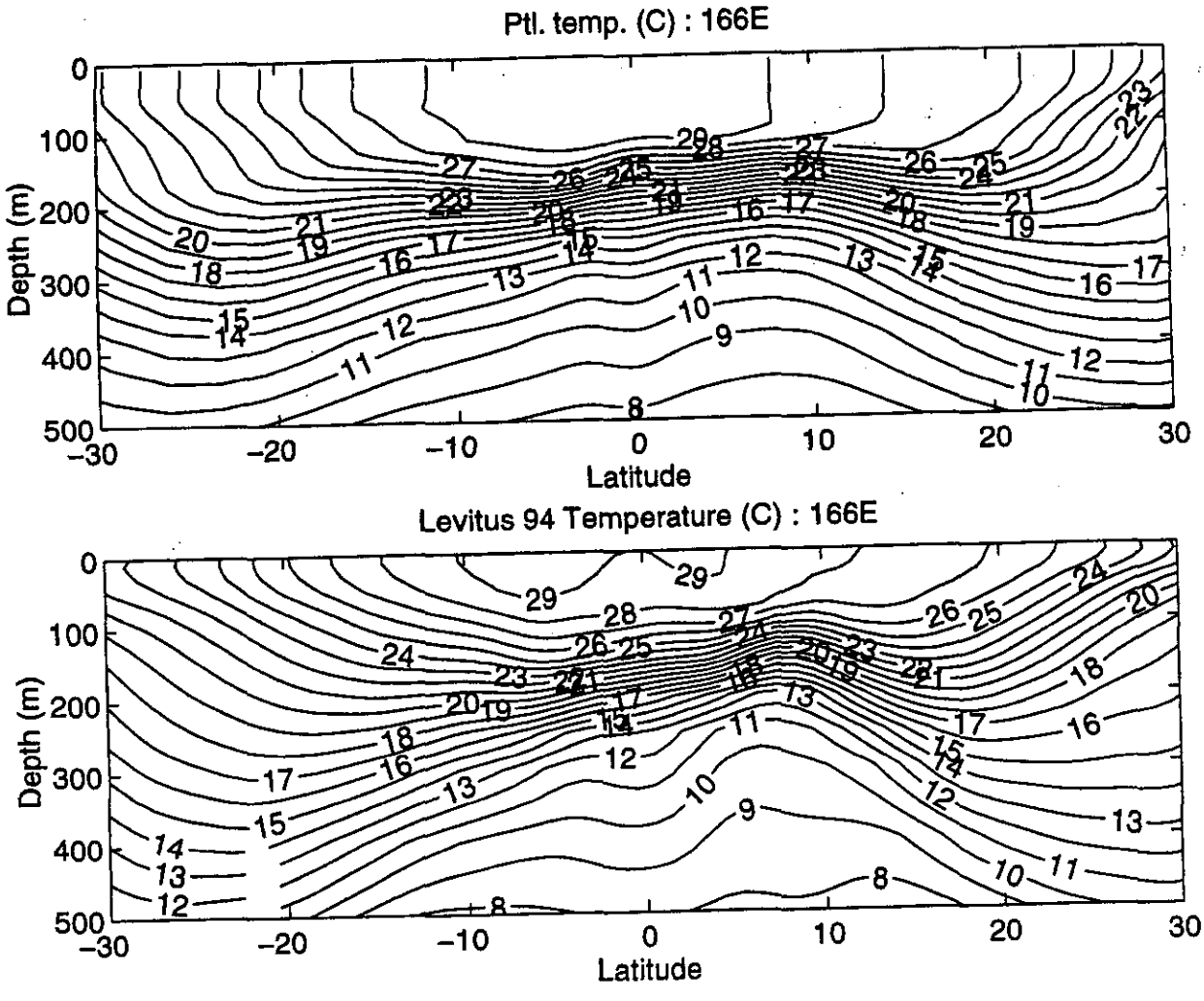

Figure 6.7: Annual mean potential temperature (°C) section along 166°E, (a) in model and (b) from Levitus and Boyer (1994).

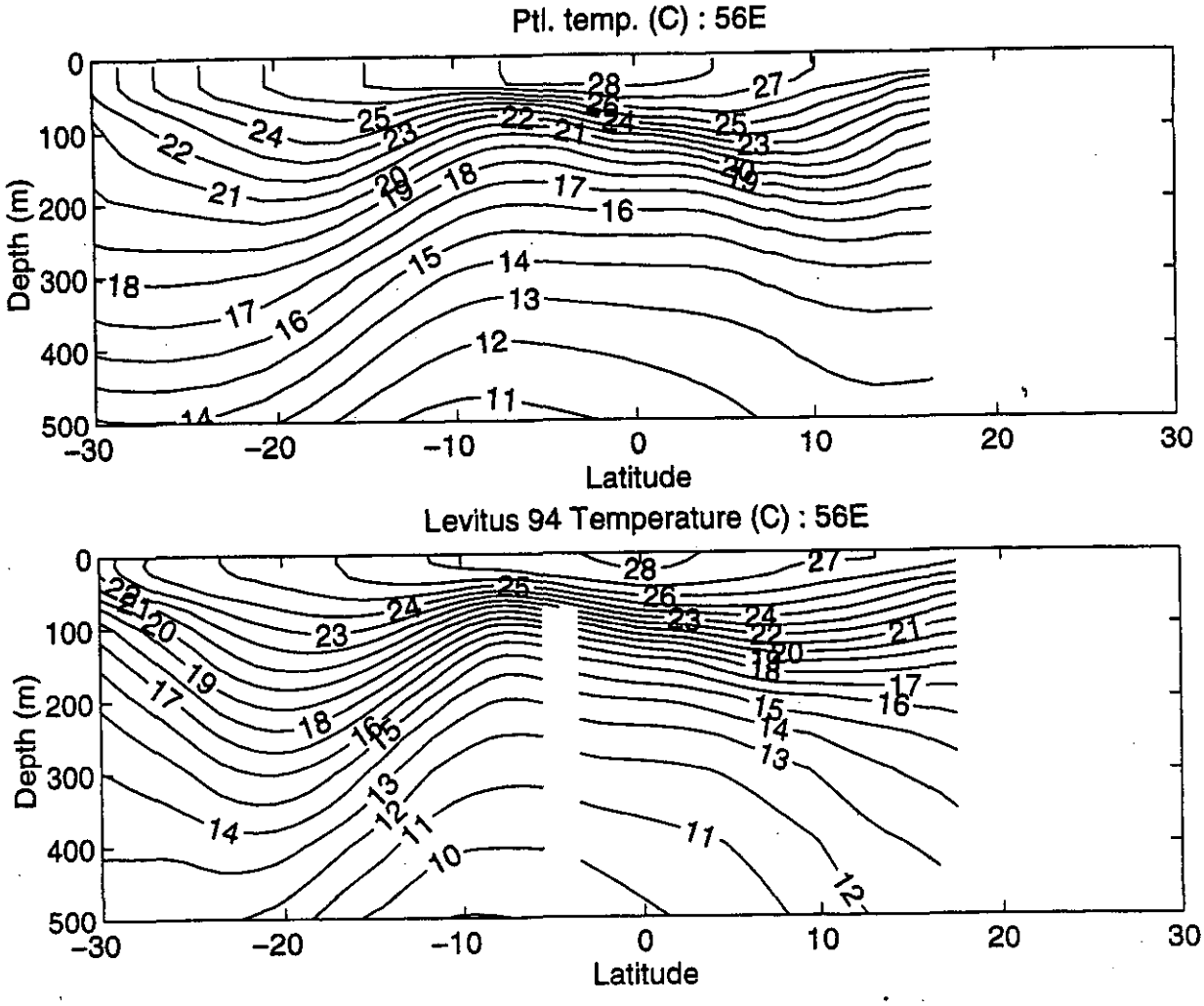

Figure 6.10: Annual mean potential temperature (°C) section along 56°E, (a) in model and (b) from Levitus and Boyer (1994).

7 Antarctic Circumpolar Current transport

The value of the Antarctic Circumpolar Current (ACC) transport in the model is given simply by the value of the barotropic streamfunction on the Antarctic coast. This is because the value of the streamfunction on the Africa/America combined continent is defined to be zero (Bering Strait is closed), and because the barotropic component of flow in the MOM code is defined so that the baroclinic component has zero depth-averaged transport.

The ACC transport during the 20 year spinup run is shown in Figure 7.1. It shows a steady decrease from an initial value of 89 Sv to 38 Sv after 20 years. The initial value is presumably set by the model's response to the thermohaline forcing implied by the Levitus initial conditions. The steady decrease is due to a combination of factors.

First, the horizontal viscosity is relatively large ($2 - 3 \times 10^5$ m^2/s) in the Southern Ocean because of the coarser grid there.

Second, the horizontal diffusivity is relatively large, being 4000 m^2/s everywhere in the model. Power (personal communication) has experimented with a coarse-resolution R21 12-level version of MOM to examine the sensitivity of the ACC transport to diffusivity. He found that with a horizontal diffusivity of 500 m^2/s, the transport was 100 Sv, while with a diffusivity of 10,000 m^2/s, the transport reduced to 23 Sv.

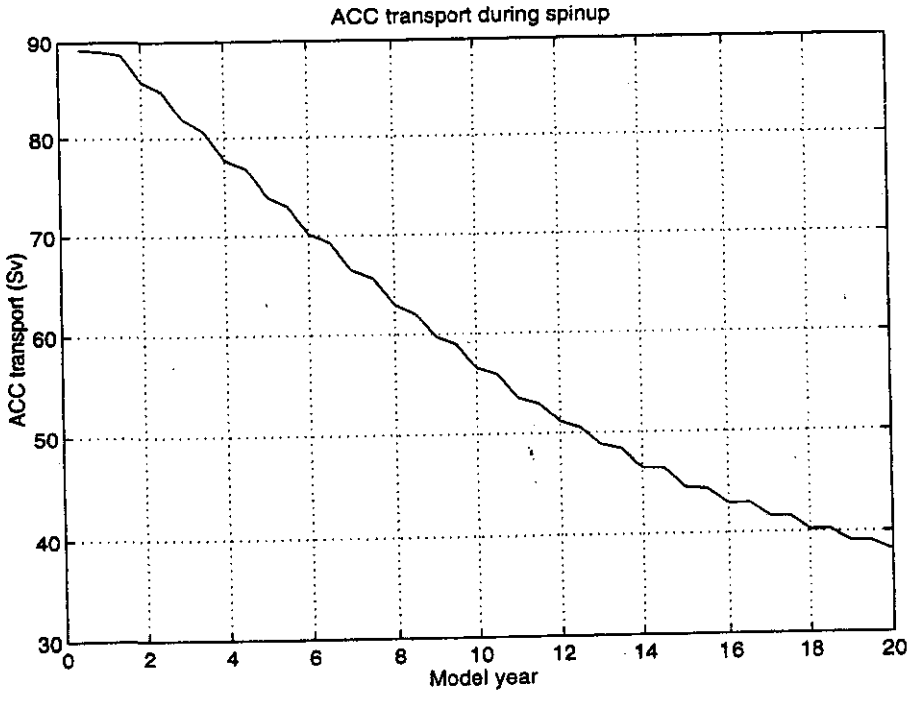

Figure 7.1: ACC transport during the 20 year spinup run.

These results are consistent with those obtained with the present model. England (1993) conducted similar experiments. He found that if the surface value decreases from 5000 m^2/s to 1000 m^2/s, the ACC transport increases from 134 to 145 Sv. The decreased sensitivity is probably due to England's horizontal diffusivity decreasing with depth, reducing the effect of changes.

Third, the surface fluxes of heat and particularly salt are unlikely to be very accurate at high latitudes. England (1993) found that adjusting the wintertime salinity around Antarctica to values that are more reasonable than the summer-biased Levitus values increases the ACC transport from 125 to 147 Sv.

Fourth, the geometry of Drake Passage may be important. However, as shown in Figure 7.2, the model Drake Passage is at least as wide as the real channel, so there is no restriction here.

In the ACC transport depicted in Figure 7.1, there is a staircase pattern superimposed on the general decrease. An integer value of model year actually coincides with February, so the greatest decrease in ACC transport occurs during the southern hemisphere spring and summer; it is not clear what this implies. Note that during the spinup run, ACC transport values were only saved every 6 months.

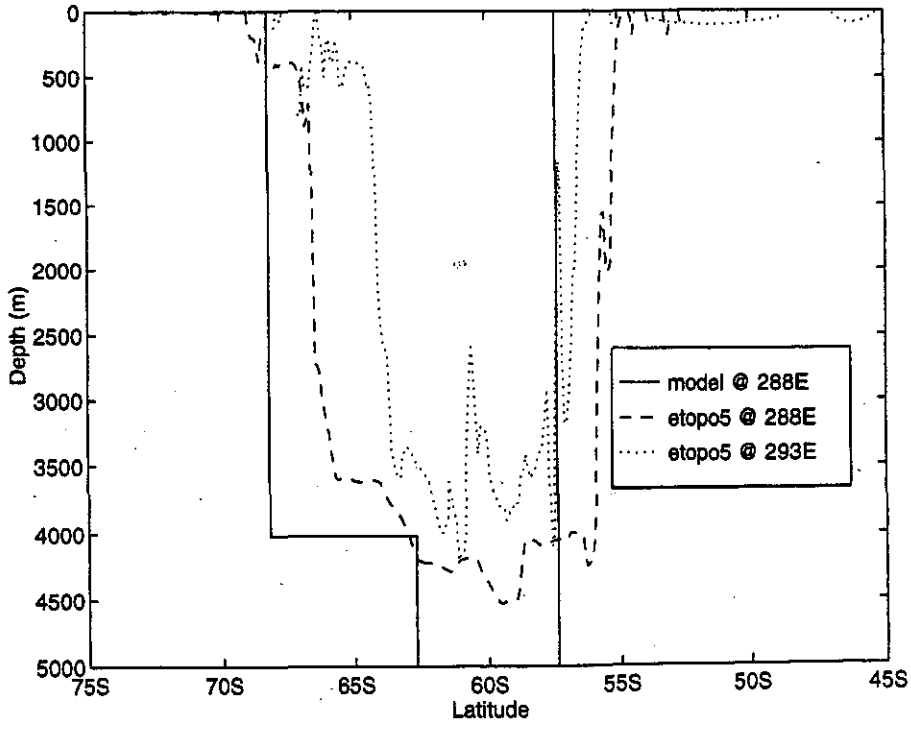

Figure 7.2: Drake passage bathymetry (ETOPO5 data set from the National Geophysical Data Center 1988) compared to the model. The model is narrowest at 288°E. The cross-section at 293°E is at approx. the narrowest point of the real channel.

In a subsequent experiment, the surface heat-flux boundary condition was changed so that the Seager et al. (1988) formula applied at all latitudes. In the spinup run, there was a gradual change from the Seager formula to relaxation to SST from 30 to 40 degrees. The experiment also changed the viscosity in Lombok Strait, but this should not affect the ACC transport. The ACC transport for this experiment is shown in Figure 7.3. Values are now available every month. The ACC transport is increasing gradually, at a rate of about 1 Sv per year (compared to an average decrease in the spinup run of about 2.5 Sv per year).

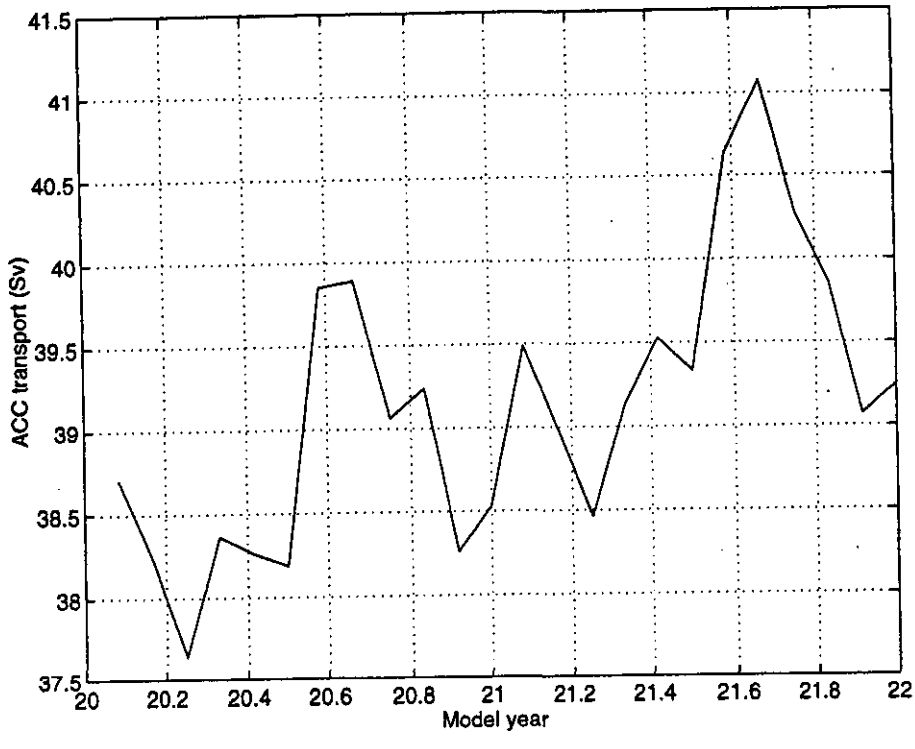

Figure 7.3. ACC transport during 2-year experiment (after 20-year spinup run).

It will be interesting to re-run the spinup with Seager forcing everywhere. It may be that the ACC transport will not decrease as much as in the original spinup. If this is so, at least part of the reduced ACC transport can be attributed to inaccurate thermal surface boundary conditions.

8 Depth-integrated steric heights

The Sverdrup relation for the annual mean, depth-integrated steric height:

$$g\frac{\partial P}{\partial x} = \frac{\tau^{(x)}}{\rho} + \frac{f}{\beta}\, curl\left(\frac{\tau}{\rho}\right) \tag{8.1}$$

provides a convenient means of testing the efficacy of the choice of bulk transfer coefficient C_D in the formula:

$$\tau = \rho_a C_D |W| \mathbf{u} \tag{8.2}$$

where τ is the wind stress, $\mathbf{u}$ the wind vector at a standard height and W the magnitude of $\mathbf{u}$. In (8.1), g is the acceleration due to gravity, P is the depth-integrated steric height (m^2), f is the Coriolis parameter and β its meridional gradient. Equation (8.1) shows that the gradients of P — unlike those of other variables, such as steric height or the depth of a particular isopycnal — do not depend on eddy diffusivities or viscosities; apart from the wind vector itself, they depend only on the bulk transfer coefficient C_D. This is convenient, because there is some controversy over the appropriate value of C_D. Harrison (1989) evaluated a global wind climatology, using the Large and Pond (1981) values for C_D; Harrison found that his climatological winds were about 0.75 times those of Hellerman and Rosenstein (HR hereafter, 1983). Godfrey (1989) obtained a global estimate of annual mean P from (8.1) and HR winds, and compared it with observed values, relative to 1500 db (Fig. 8.1b). The HR estimates of gradient in the subtropical gyres were consistently larger than observed values, in agreement with Harrison (1989), though not by as much as Harrison found. However, along the equatorial Pacific — a region of special importance for climate modelling — the HR estimate matched observed values of P remarkably well (Fig. 8.2b). Stockdale et al. (1993) compared several Pacific Ocean models; all were driven by HR winds multiplied by 0.75, the factor 0.75 apparently deriving from Harrison's work.

We have used FSU pseudostresses with a constant bulk transfer coefficient of 0.0015. To test this choice, we calculated depth-integrated steric height relative to 1009 m. Figure 8.1a shows (ρg) times the annual mean depth-integrated steric height P for our model with our choice of C_D, using the seasonal mean of FSU winds over 1985–1990. Depth-integrated steric heights in m^2 are obtained from the numbers appearing along the contours in Figure

8.1a and multiplying by 100. Only horizontal differences in Figure 8.1a,b are physically significant, not absolute values.

For comparison, Figure 8.1b shows the observed long-term mean depth-integrated steric heights relative to 1500 db from Godfrey (1989). In general — noting that the contour interval in Figure 8.1a is 25 m^2, while that in Figure 8.1b is 50 m^2 — the agreement is good globally, indicating that our choice of 0.0015 for the bulk transfer coefficient is reasonable. Note also that no drastic effects are seen in Figure 8.1a near 30°N, 30°S, where we change wind products. This might be expected to generate spurious wind stress curls at these latitudes, but if it does so they are not large.

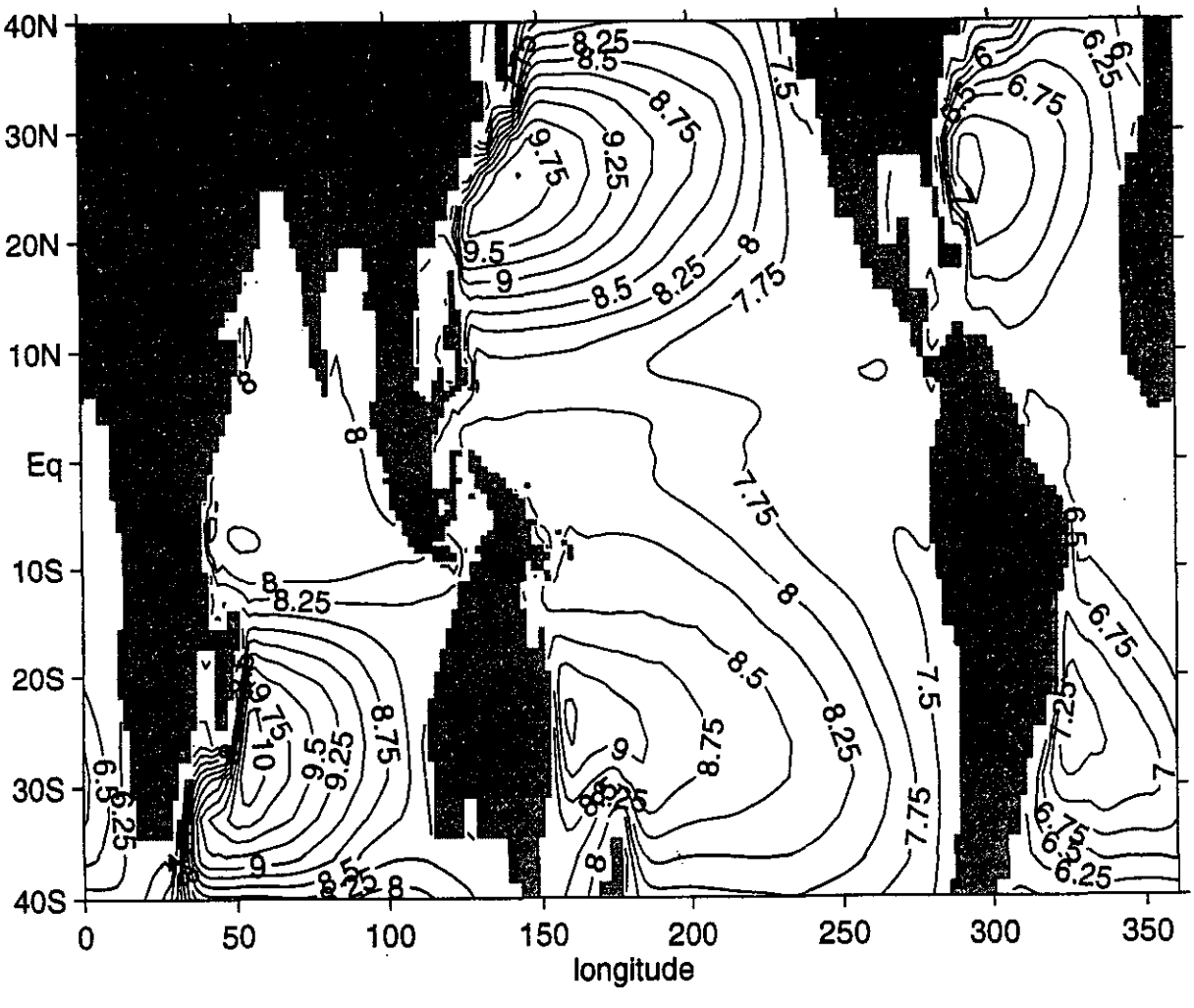

Figure 8.1a: Annual mean depth-integrated steric height relative to 1009 m from the model. Numbers appearing on contours should be multiplied by 100 to obtain depth-integrated steric height in m^2, i.e. contour interval is 25 m^2. An arbitrary additive constant may be removed from this field.

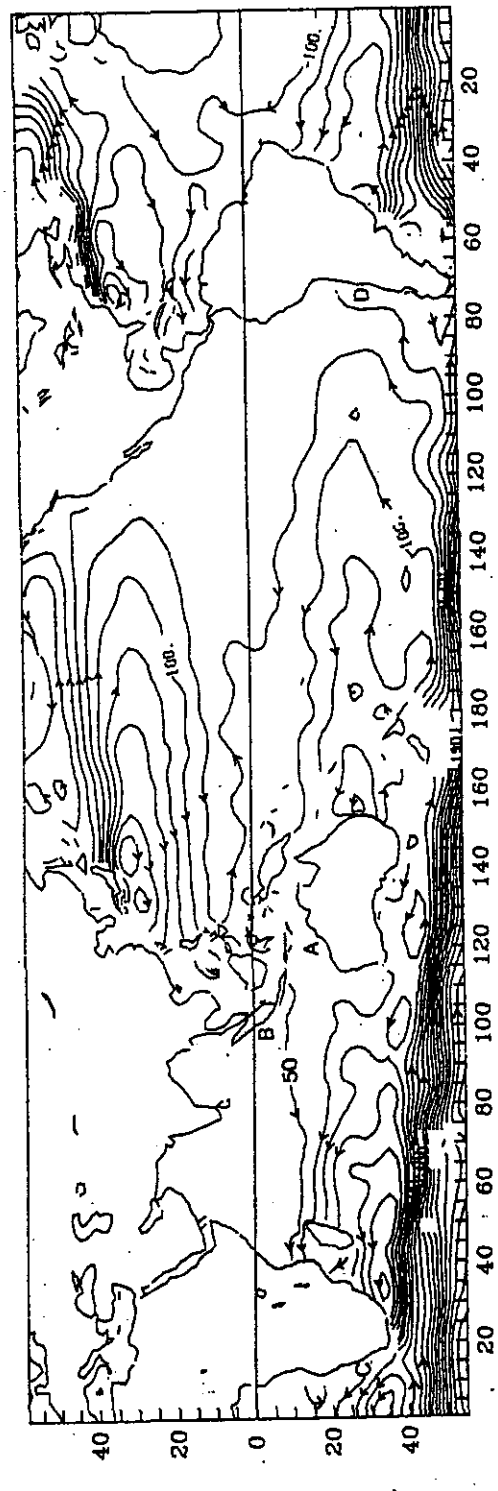

Figure 8.1b: Annual mean depth-integrated steric height relative to 1500 db, based on Levitus data (1982). Source: Godfrey (1989).

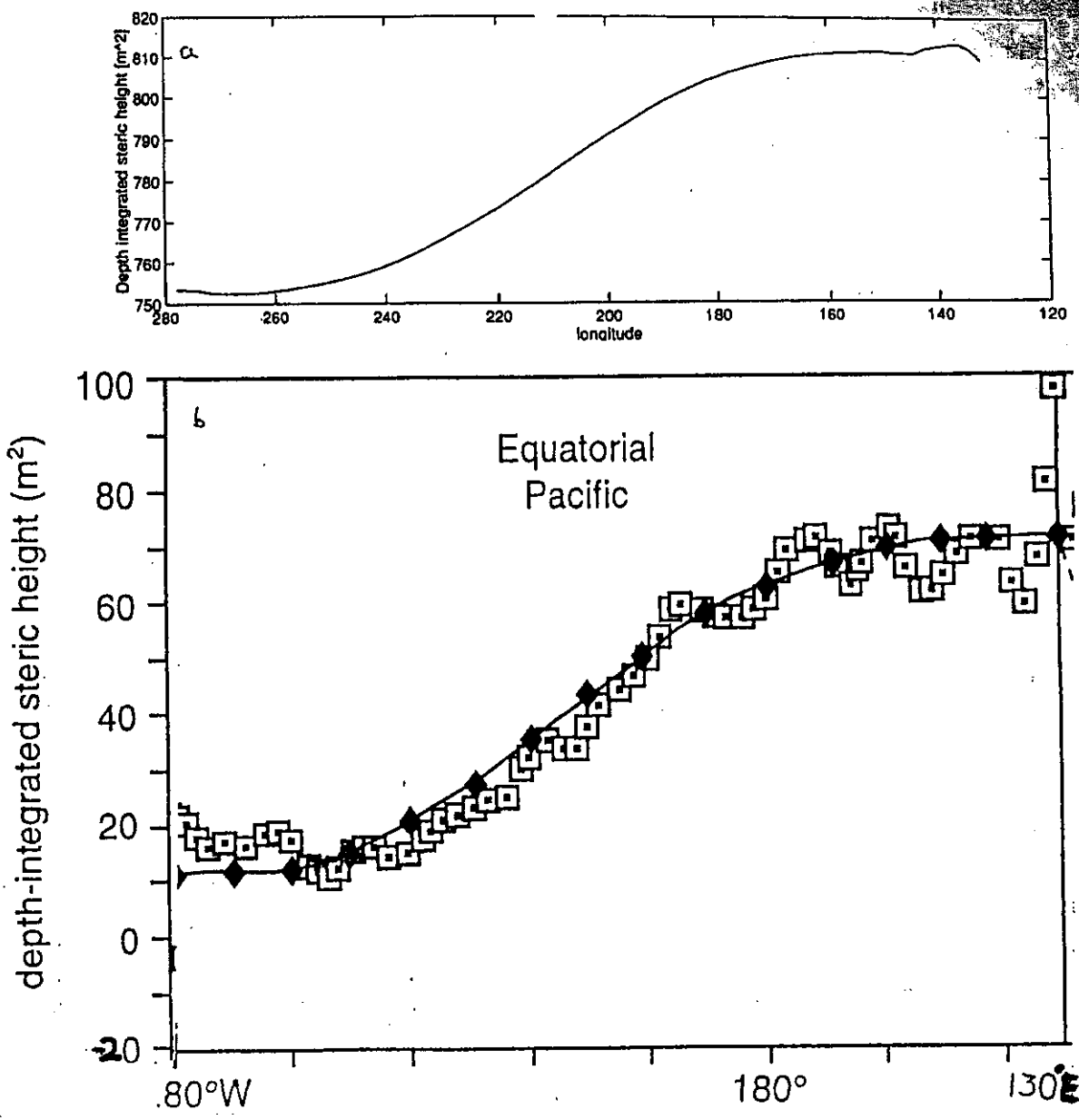

Figure 8.2a: Annual mean depth-integrated steric height relative to 1009 m from the model, along the equatorial Pacific.

Figure 8.2b: Squares denote annual mean depth-integrated steric height relative to 1000 db from the observations of Levitus (1982), along the equatorial Pacific. Diamonds denote the progressive integral $\int_{x_E}^{x} \tau^{(x)} dx/g\rho$ along the equator, for annual mean Hellerman and Rosenstein (1983) winds.

A stronger test of the validity of C_D is obtained by comparing the model's value of depth-integrated steric height with the observed values relative to 1000 db from Levitus (1982), along the equatorial Pacific. The latter is shown by squares in Figure 8.2b — adapted from Godfrey (1996). The full line in Figure 8.2b is the progressive integral: $\int_{x_E}^{x} \tau^{(x)} dx/g\rho$ along the equator, for Hellerman and Rosenstein (1983) winds. The good agreement of the line and squares in the equatorial Pacific suggests (a) that (8.1) is valid along the equator and (b) that the Hellerman and Rosenstein (1983) bulk transfer coefficient is fairly accurate, at least in the equatorial Pacific.

Figure 8.2a shows the depth-integrated steric height from the model, relative to 1009 m. Disregarding the "bump" near 130° E, which is probably associated with nonlinearity of the modelled western boundary current near Irian Jaya (e.g. Godfrey 1996), the model shows a net rise in depth-integrated steric height from east to west across the Pacific of close to 60 m^2. This is almost exactly the rise in the observations. We conclude that our choice of bulk transfer coefficient is appropriate.

9 Tidal mixing

Particular attention in our model is given to the Indonesian Throughflow area because it is the only low-latitude connection between two major oceans and because SST in this region has been shown to affect Australia's rainfall. As water flows from the Pacific to the Indian Ocean, the tidally induced vertical mixing in the Indonesian archipelago is able to change the water-mass structure of the Indian Ocean significantly (Ffield and Gordon 1992). A recent analysis by Ffield and Gordon (1996) suggests that the centre of the tidal-mixing effect on SST is in the Banda Sea (Fig. 9.1a,b). To simulate this observed feature, we increased the vertical mixing coefficients (diffusion and viscosity) in the Indonesian area. This was done by defining a spatial Gaussian function similar to the sum of Figures 9.1a and b, which describes the spatial shape of the additional vertical mixing. The centre of the additional "tidal mixing" in the model is in the Banda Sea. It has a maximum value of $2 \times 10^{-4}\,m^2/s$; which gradually decreases as the distance from the Banda Sea increases. The additional mixing is independent of time (i.e. we made no attempt to resolve the timescales associated with its physical origin). We are only concerned with its larger time-scale effects on SST.

The difference between the model's and observed SST is shown for two experiments, one with and one without tidal mixing (Fig. 9.2). Because the eastern Indian Ocean is strongly affected by the Indonesian Throughflow, it is particularly this region where the tidal mixing reduces the SST differences by more than 0.4 °C (Fig. 9.2b) compared to the experiment without any tidal mixing (Fig. 9.2a). The inclusion of tidal mixing almost halves the model–data misfit in SST.

Furthermore, the annually averaged surface heat-flux changes sign in part of the area affected by the tidal mixing (Fig. 9.3). The tidal mixing causes lower SSTs and thus the Timor Sea gains heat, typically about -50 W/m^2, which is consistent with estimates based on observations (Oberhuber 1988). Due to the additional heat, the ocean gains buoyancy which reduces the mixed-layer depth (not shown).

Due to the short integration time of 2 years for the tidal mixing experiment described above, the signal of the modified water masses could not penetrate into the whole Indian Ocean. To investigate its effects on the Indian Ocean water-mass properties, an extended integration with tidal mixing in the Indonesian area is under way.

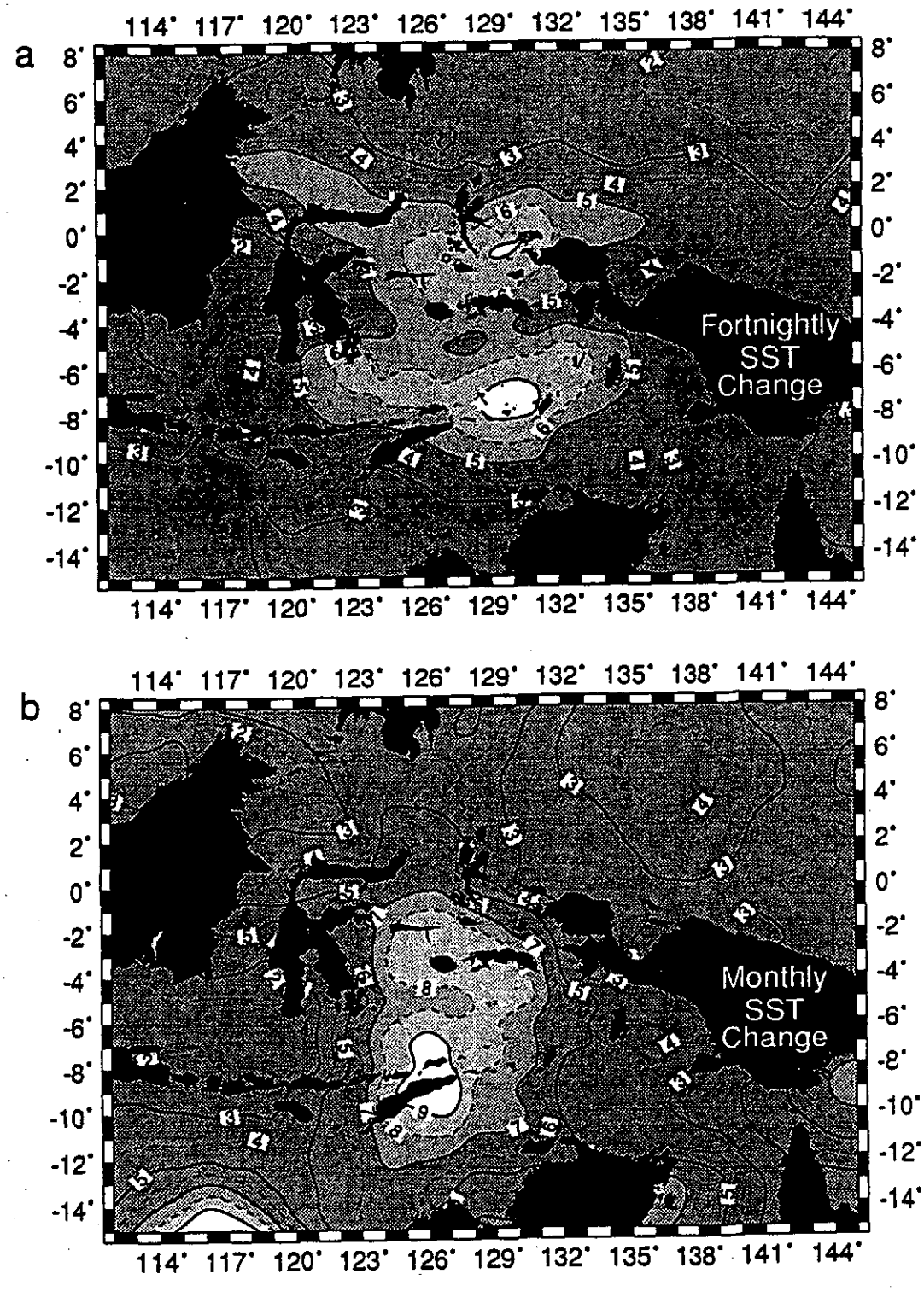

Figure 9.1: Power spectral density estimates in the (a) fortnightly and (b) monthly bandwidths of the weekly change in sea-surface temperature calculated for each one degree square. The units of the contours are $(°C/week)^2$. From Ffield and Gordon (1996).

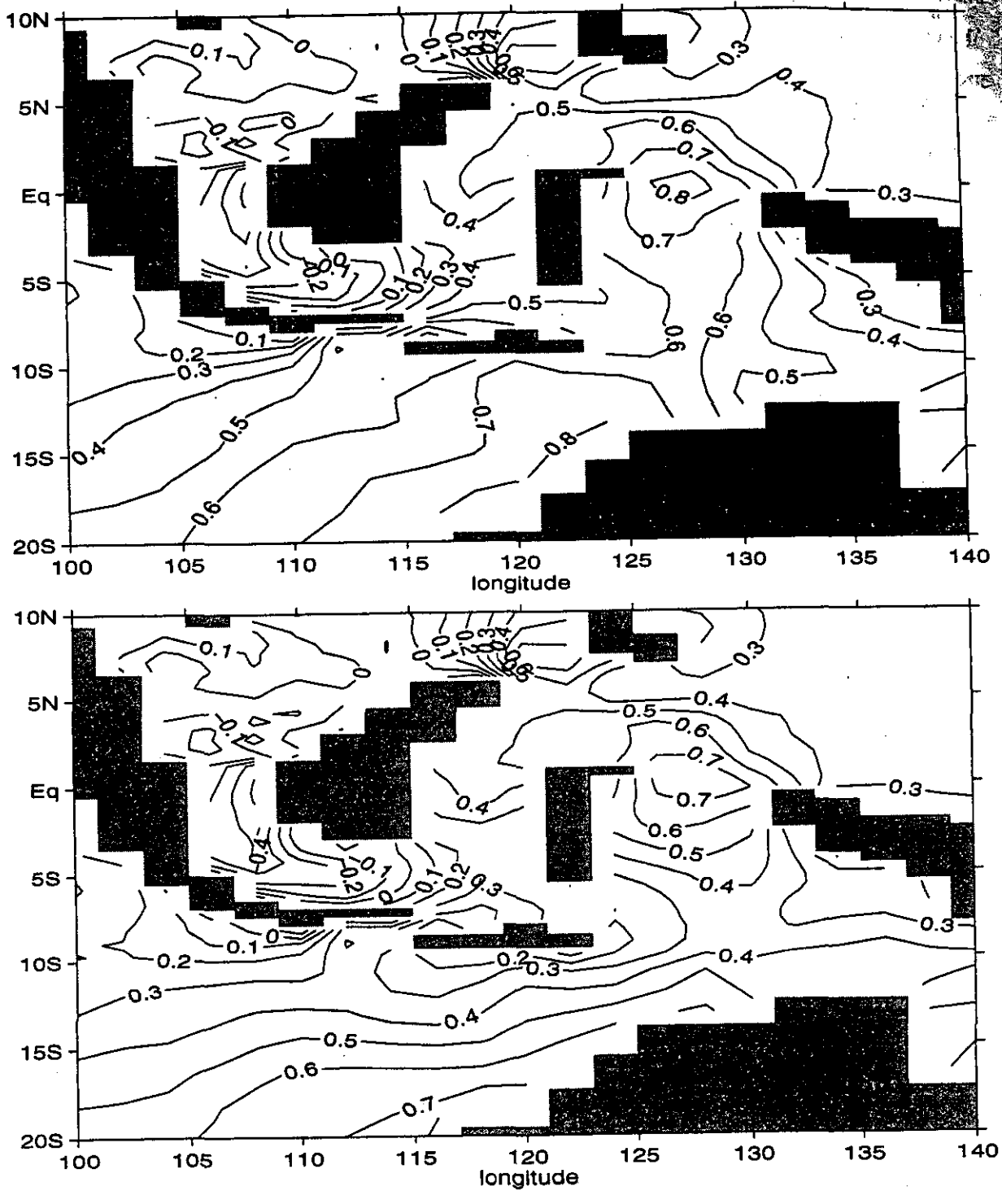

Figure 9.2: Annual mean SST differences (model minus observations) for (a) experiment without tidal mixing and (b) experiment with tidal mixing. Units are in °C.

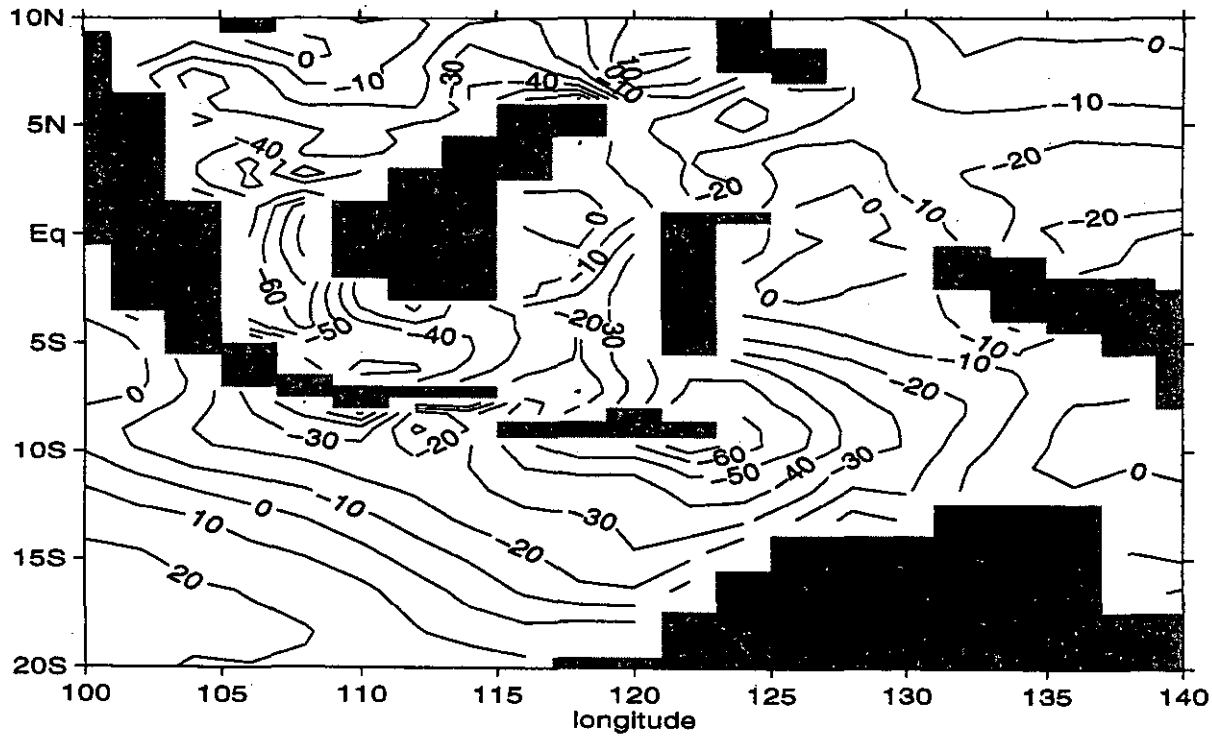

Figure 9.3: Annual mean heat-flux difference (W/m^2) between experiments with and without tidal mixing.
Negative values denote additional heat gain of the ocean.

Acknowledgements:
We wish to thank R. Pacanowski from the Geophysical Fluid Dynamics Laboratory for making the MOM2 code available to us. Russell Fiedler and Michael Bessell helped us prepare the figures. Steve Wilson and Ken Ridgway are thanked for their comments on the manuscript. Thanks to Vivienne Mawson for carefully editing the manuscript. During the development of this model we had many helpful discussions with colleagues at the CSIRO Division of Atmospheric Research and the Bureau of Meteorology Research Centre. In particular, we appreciated the comments of Steve Wilson, Scott Power, Richard Kleeman, Tony Hirst, Neville Smith and Linda Waterman.
This project was partly supported by funding from the Department of Industry, Sciences and Technology (CSIRO Climate Variability and Impacts Program) and by a grant from the Land & Water Resources Research and Development Corporation.

10 References

Chen, D., L.M. Rothstein and A.J. Busalacchi, 1994a. A hybrid vertical mixing scheme and its application to tropical ocean models. J. Phys. Oceanog., 24, 2156-2179.

Chen, D., A. Busalacchi and L.M. Rothstein, 1994b. The roles of vertical mixing, solar radiation, and wind stress in a model simulation of the sea surface temperature seasonal cycle in the tropical Pacific Ocean. J. Geophys. Res., 99, 20345-20359.

Cresswell G.R., A. Frische, J. Peterson and D. Quadfasel, 1993. Circulation in the Timor Sea. J. of Geophys. Res., 98, 14,379-14,389.

Delcroix, T., G. Eldin and C. Henin, 1987. Upper ocean water masses and transport in the western tropical Pacific (165°E). J. Phys. Oceanogr., 17, 2248-2262.

Donguy, J.R. and G. Meyers, 1996. Seasonal variations of sea-surface salinity and temperature in the tropical Indian Ocean. Deep–Sea Res., 42, 1007-1028.

Drosdowsky, W., 1993. An analysis of Australian seasonal rainfall anomalies: 1950-1987. II: Temporal variability and teleconnection patterns. Int. J. Climatol., 13, 111-149.

England, M.H., 1993. Representing the global-scale water masses in ocean general circulation models. J. Phys. Oceanogr., 23, 1523-1552.

Ffield, A. and A.L. Gordon, 1992. Vertical mixing in the Indonesian thermocline. J. Phys. Oceanogr., 22, 184-195.

Ffield, A. and A.L. Gordon, 1996. Tidal mixing signatures in the Indonesian seas, J. Phys. Oceanogr., 26, 1924-1937.

Gates, W.L. and A.B. Nelson, 1975. A new (revised) tabulation of the Scripps topography on a 1° global grid. Part I. Terrain heights. Tech. Rep. R-1276-1-ARPA, The RAND Corporation, 132 pp.

Godfrey, J.S., 1989. A Sverdrup model of the depth-integrated flow for the world ocean allowing for island circulations. Geophys. Astrophys. Fluid Dyn., 45, 89-112.

Godfrey, J.S., 1996. The effect of the Indonesian Throughflow on ocean circulation and heat exchange with the atmosphere: a review. J. Geophys. Res., 101, 12217-12237.

Godfrey, J.S. and A. Schiller, 1997. Tests of mixed layer schemes and surface boundary conditions in an ocean general circulation model, using an equatorial data set. CSIRO Report, in press.

Harrison, E., 1989. On climatological monthly mean wind stress and wind stress curl fields over the World Ocean. J. Climate, 2, 57-70.

Hastenrath, S. and L. Greischar, 1991. The monsoonal current regimes of the Tropical Indian ocean. Observed surface flow fields and their geostrophic and wind-driven components. J. Geophys. Res., 96, 12619-12633.

Hellerman, S. and M. Rosenstein, 1983. Normal monthly wind stress over the World Ocean with error estimates. J. Phys. Oceanogr., 13, 1093-1104.

Kleeman, R. and S.B. Power, 1995. A simple atmospheric model of surface heat flux for use in ocean modelling studies. J. Phys. Oceanogr., 25, 92-105.

Large, W.G. and S. Pond, 1981. Open ocean momentum flux observations in moderate to strong winds. J. Phys. Oceanogr. 11, 324-336.

Legler, D.M., I.M. Navon and J.J. O'Brien, 1989. Objective analysis of pseudostress over the Indian Ocean using a direct-minimization approach. Month. Weath. Rev., 117, 709-720.

Levitus, S., 1982. Climatological atlas of the world ocean. NOAA Prof. Paper No. 13, 173 pp.

Levitus, S. and T.P. Boyer, 1994. World ocean atlas 1994, vol. 4: Temperature. NOAA Atlas NESDIS 4. U.S. Government Department of Commerce, NOAA, NESDIS, Washington, D.C.

Li, Z., 1995. Intercomparison between two satellite-based products of net surface radiation. J. Geophys. Res., 100, 3221-3232.

Luyten, J.R. and D.H. Roemmich, 1982. Equatorial currents at semiannual period in the Indian Ocean. J. Phys. Oceanogr., 12, 406-413.

Masuzawa, J., 1969. Subtropical Mode Water. Deep–Sea Res. 16, 463-472.

McPhaden, M.J., 1982. Variability in the central equatorial Indian Ocean Part 1: Ocean dynamics. J. Mar. Res. 40, 157-176.

McPhaden, M.J., A.J. Busalacchi, R. Cheney, J.-R. Donguy, K.S. Gage, D. Halpern, M. Ji, P. Julian, G. Meyers, G.T. Mitchum, P.P. Niiler, J. Picaut, R.W. Reynolds, N. Smith and K. Takeuchi, 1997. The Tropical Ocean Global Atmosphere (TOGA) Observing System: A Decade of Progress. J. Geophys. Res., (submitted).

Mechoso, C.R., A.W. Robertson, N. Barth, M.K. Davey, P. Delecluse, P.R. Gent, S. Ineson, B. Kirtman, M. Latif, H. Le Treut, T. Nagal, J.D. Neelin, S.G.H. Philander, J. Polcher, P.S. Schopf, T. Stockdale, M.J. Suarez, L. Terray, O. Thual and J.J Tribbia, 1995. The seasonal cycle over the tropical Pacific in coupled ocean–atmosphere general circulation models. Monthly Weather Rev., 123, 2825-2838.

Meyers, G., R.J. Bailey, and A.P. Worby, 1995. Geostrophic transport of Indonesian Throughflow. Deep Sea Res., 42, 1163-1174.

Molinari, R.L., D. Olson and G. Reverdin, 1990. Surface current distributions in the Tropical Indian Ocean derived from compilations of surface buoy trajectories. J. Geophys. Res., 95, 7217-7238.

Murray, S.P. and D. Arief, 1988. Throughflow into the Indian Ocean through the Lombok Strait, January 1985–January 1986. Nature, 333, 444-447.

National Geophysical Data Center, 1988. ETOPO5 Bathymetry/Topography Data, United States Department of Commerce, Boulder, U.S.A.

Neelin, N.D., M. Latif, M.A.F. Allaart, M.A. Cane, U. Cubasch, W.L. Gates, P.R. Gent, M. Ghil, C. Gordon, N.C. Lau, C.R. Mechoso, G.A. Meehl, J.M. Oberhuber, S.G.H. Philander, P.S. Schopf, K.R. Sperber, A. Sterl, T. Tokioka, J. Tribbia and S.E. Zebiak, 1992. Tropical air–sea interaction in general circulation models. Clim. Dyn., 7, 73-104.

Nicholls, N., 1989. Sea surface temperatures and Australian winter rainfall. J. Climate, 2, 965-973.

Niiler, P.P. and E.B. Kraus, 1977. One-dimensional models of the upper ocean. In: E.B. Kraus (Ed.): Modeling and prediction of the upper layers of the ocean. Pergamon Press, Oxford, 143-172.

Oberhuber, J.M., 1988. An atlas based on the 'COADS' data set: The budgets of heat, buoyancy and turbulent kinetic energy at the surface of the global ocean. Max-Planck-Institute of Meteorology, Report No.15.

Pacanowski, R. and S.G.H. Philander, 1981. Parameterisation of vertical mixing in numerical models of tropical oceans. J. Phys. Oceanogr., 11, 1443-1451.

Pacanowski, R.C., 1995. MOM2 Documentation User's Guide and Reference Manual, Version 1.0, GFDL Technical Report No. 3.

Peters, H., M.C. Gregg and J.M. Toole, 1988. On the parametrization of equatorial turbulence. J. Geophys. Res., 93, 1199-1218.

Power, S.B., R. Kleeman, F. Tseitkin and N.R. Smith, 1995. On a global version of the GFDL Modular Ocean Model for ENSO studies. BMRC Technical Report.

Rao, R.R., R.L. Molinari and J.F. Festa, 1989. Evolution of the climatological near-surface thermal structure of the tropical Indian Ocean. 1. Description of mean monthly mixed layer depth, and sea surface temperature, surface current, and surface meteorological fields. J. Geophys. Res., 94, 10801-10815.

Reynolds, R.W., 1988. A real-time global sea surface temperature analysis, J. of Climate, 1, 75-86.

Reynolds, R.W. and T.M. Smith, 1994. Improved global sea surface temperature analyses using optimum interpolation. J. Climate, 7, 929-948.

Robinson, M.K., 1976. Atlas of North Pacific ocean monthly mean temperatures and mean salinities of the surface layer. Ref. Publ. 2, Naval Oceanographic Office, Washington, D.C.

Robinson, M.K., R.A. Bauer and E.H. Schroeder, 1979. Atlas of North Atlantic-Indian Ocean ocean monthly mean temperatures and mean salinities of the surface layer. Ref. Publ. 18, Naval Oceanographic Office, Washington, D.C.

Seager, R., S.E. Zebiak, and M.A. Cane, 1988. A model of the tropical Pacific sea surface climatology. J. Geophys. Res., 93, 1265-1280.

Simonot, J.-Y. and H.L. Le Treut, 1986. A climatological field of mean optical properties of the world ocean. J. Geophys. Res., 91, 6642-6646.

Sprintall, J. and M. Tomczak, 1992. Evidence of the barrier layer in the surface layer of the tropics. J. Geophys. Res., 97, 7305-7316.

Stockdale, T., D. Anderson, M. Davey, P. Delecluse, A. Kattenberg, Y. Kitamura, M. Latif and T. Yamagata, 1993. TOGA Numerical Experimentation Group: Intercomparison of Tropical Ocean GCMs. World Climate Research Publication WCRP-79.

Stricherz, J.N., J.J. O'Brien and D.M. Legler, 1992. Atlas of Florida State University tropical Pacific winds for TOGA 1966-1985. Florida State University. 256 pp.

Wijffels, S.E., N. Bray, S. Hautala, G. Meyers and W.M.L. Morawitz, 1996. The WOCE Indonesian throughflow repeat hydrography sections: I10 and IR6. WOCE Newsletter, 24, 25-28.

Wyrtki, K., 1971. Oceanographic atlas of the International Indian Ocean Expedition. National Science Foundation, Washington, D.C.

Wyrtki, K. and B. Kilonsky, 1984. Mean water and current structure during the Hawaii to Tahiti Shuttle Experiment. J. Phys. Oceanogr., 14, 242-254.

CSIRO Marine Laboratories

Division of Marine Research
(formerly the Division of Fisheries and the Division of Oceanography)

Headquarters
Castray Esplanade, Hobart, Tasmania 7001
GPO Box 1538, Hobart, Tasmania 7001, Australia

Queensland Laboratory
133 Middle Street, Cleveland, Queensland 4163
PO Box 120, Cleveland, Queensland 4163, Australia

Western Australia Laboratory
Leach Street, Marmion, W.A.
PO Box 20, North Beach, W.A. 6020, Australia

ISBN 0 643 05959 8
ISSN 0725–4598